A stochastic cellular automaton model to describe the evolution of the snow-covered area across a high-elevation mountain catchment

# A stochastic cellular automaton model to describe the evolution of the snow-covered area across a high-elevation mountain catchment

Kevin J. Painter, Alessio Gentile, Stefano Ferraris

[a]*Interuniversity Department of Regional and Urban Studies and Planning (DIST), Politecnico di Torino, Viale Pier Andrea Mattioli, Torino, 10125, Piedmont, Italy*

**Abstract**

Variations in the extent and duration of snow cover impinge on surface albedo and snowmelt rate, influencing the energy and water budgets. Monitoring snow coverage is therefore crucial for both optimising the supply of snowpack-derived water and understanding how climate change could impact on this source, vital for sustaining human activities and the natural environment during the dry season.

Mountainous sites can be characterised by complex morphologies, cloud cover and forests that can introduce errors into the estimates of snow cover obtained from remote sensing. Consequently, there is a need to develop simulation models capable of predicting how snow coverage evolves across a season. *Cellular Automata* models have previously been used to simulate snowmelt dynamics, but at a coarser scale that limits insight into the precise factors driving snowmelt at different stages.

To address this information gap, we formulate a novel, fine-scale stochastic Cellular Automaton model that describes snow coverage across a high-elevation catchment. Exploiting its refinement, the model is used to explore the interplay between three factors proposed to play a critical role: terrain elevation, sun incidence angle, and the extent of nearby snow. We calibrate the model via a randomised parameter search, fitting simulation data against snow cover masks estimated from Sentinel-2 satellite images. Our analysis shows that:

- the three simple assumptions are sufficient to yield a close correspondence between model output and the estimated snow cover masks ;
- across the study area, elevation and neighbouring snow appear to be particularly influential, with incidence playing a relatively minor role for much of the process ;
- incidence, though, plays a significant role early in the process, and allows the identification of regions that receive sufficient solar energy to trigger snowmelt ;
- discrepancies between model output and satellite data indicate other potential factors at play, the identification of which will demand future attention.

*Keywords:* High-Elevation Catchment, Snow Cover Area, Sentinel-2, Cellular Automaton Model, Mountain Hydrology
*2010 MSC:* 86A05
*2010 MSC:* 86-08

## 1. Introduction

Water related problems range from scarcity to flooding, calling for a variety of modelling and predictive approaches that can include rainfall-runoff models (Ditthakit et al. 2021) or the adoption of machine learning techniques (Singh et al. 2022, Mohammadi et al. 2022). In a high-mountain environment, the seasonal snowpack constitutes a key resource, providing a delayed and steady water source that contributes significantly to the hydrological cycle, therefore demanding careful modelling (Jenicek and Ledvinka 2020, Leavesley 1989). In particular, snowmelt recharges

groundwater storage (Cochand et al. 2019), fundamental for supplies of drinking water, along with industry and agriculture (Dietz et al. 2012). For countries with an abundance of hydropower, the seasonal snowpack also constitutes a valuable renewable energy stock (Vikhamar and Solberg 2003). As a consequence, monitoring and simulating annual and seasonal variation in snow cover is vital to understand both the availability and the sustainable management of this crucial water source (Butt and Bilal 2011, Pardo-Igúzquiza et al. 2017), hence contributing to *Sustainable Development Goal 6 (SDG6)*. Further, water management has become increasingly topical in the light of climate change (Collados-Lara et al. 2021), *SDG13*. High-elevation environments are particularly sensitive to climate change, and its consequences can be rapidly perceived. Rising temperatures increase the solar radiation absorbed by the snowpack, thereby amplifying the initial warming and altering the surface albedo (Thackeray and Fletcher 2016). This in turn leads to earlier melting (Xiao 2021), in advance of the driest season when the demand for water is acute, particularly so given the increasing frequency of droughts (Faye 2022). These processes have repercussions for the hydrological cycle (Kundzewicz 2008) and demand exploration into whether these planetary-scale changes are reversible or not: *"Is the hydrological cycle regionally accelerating/decelerating under climate and environmental change, and are there tipping points (irreversible changes)?"* was recently posed as one of 23 unsolved problems identified by the hydrology community (Blöschl et al. 2019).

The main focus of this paper is the *Snow-Covered Area* (*SCA*), an important variable for physically-based models that aim to compute the energy and water balance in snow-dominated environments (Barry et al. 1990). On the one hand, the *SCA* controls surface albedo and, consequently, thermal fluxes (Armstrong and Brun 2008). On the other hand, it is a necessary (but, we note, not sufficient) input for simulating the runoff due to snowmelt (DeWalle and Rango 2008) and how this could change under different climate change scenarios. For example, we refer to Javadinejad et al. (2020); Kumar et al. (2022) for regionally-specific changes in the snowmelt runoff, under various projections for altered *SCA* and/or temperature increase.

Multi-spectral satellite images have long been used in the mapping of snow cover, with *SCA* identified through the *Normalized Difference Snow Index* (*NDSI*) (Dozier 1989; Hall et al. 1995). This index exploits the distinct reflectance of snow and clouds from both visible and short-wave infrared bands (for more details, see section 2.1) and *SCA* can then be estimated by counting the pixels classified above a specified *NDSI* threshold, or via a (previously calibrated) relationship between the *NDSI* and the *fractional SCA* ($f_{SCA}$, that is the percentage of snow coverage per pixel), see Salomonson and Appel (2004). This topic has received considerable attention, albeit with different aims. For example, Liang et al. (2008) have studied the accuracy of the *MODIS* algorithm for mapping snow cover under different snow depth and land cover conditions, finding that both factors perturb the algorithm accuracy. Dedieu et al. (2016) have used *SCA* to validate estimates of the first snow-free day, obtained through calculating the *NDSI* based on remote sensing observations (*MODIS, SPOT-4/5, Landsat-8*) and comparing against ground-based measurements. Di Marco et al. (2020) have performed a comparison into *MODIS* and model-derived estimates of *SCA*, considering how the impact of land use and solar illumination conditions affect this comparison. Furthermore, the same study has identified the minimum level of incoming short-wave radiation for precise use of *MODIS SCA* in forested areas.

Manifestly, estimating and/or predicting *SCA* has numerous potential applications, yet problems persist with its determination through remote sensing. For example, Masson et al. (2018) have highlighted that for mountainous sites, characterised by complex morphologies, frequent cloud cover and forests, the identified *SCA* is typically affected by errors. This motivates the development and application of models capable of simulating snow cover dynamics within high-elevation catchments, and in particular identifying the key factors that determine snowmelt. Models of this nature can then be deployed to provide a continuous map of snow cover across a season, filling in the times when satellite images are either unavailable or patchy, e.g. due to

cloud cover.

According to application, a range of snow cover models have been developed, from simple degree-day models to complex and multi-layered snow cover evolution models (Largeron et al. 2020). Snow cover estimates from such models, though, are subject to significant uncertainty, a combination of input data errors and the simplifications necessary when implementing complicated physical processes or attempting to understand complex environments (Largeron et al. 2020). Precise mathematical modelling of snowmelt is therefore challenging, with the precise influence of the controlling factors difficult to deduce. For example, snow cover evolution within high-elevation landscapes depends on the density, grain size, and microstructure of snow, the mass and timing of snowfalls, as well as air temperature, wind, (direct and diffuse) solar radiation, and topography. Clearly, this represents a highly stochastic and complex dynamical system, making it difficult to apply models at a refined spatial level, due to the general unavailability or difficulty in introducing spatial microstructure (e.g. across a catchment area) within the input data.

*Cellular Automata* (*CA*) models have been widely used for spatial environmental modelling (Ghosh et al. 2017), in applications ranging from forest fire propagation (Karafyllidis and Thanailakis 1997) to soil erosion by water (D'Ambrosio et al. 2001). In the context of melting processes, Ma et al. (2019) employed an (*CA*-like) Ising model to describe the ponds that form during the melting of sea ice. This, though, takes place on an essentially flat surface, whereas snow cover in mountain catchments will be strongly influenced by factors like aspect and slope (Abudu et al. 2016). The potential of *CA* approaches for describing *SCA* dynamics has been highlighted by Leguizamón (2005), advantages including their formulation without precise (and difficult to apply) mathematical formulae and ease of simulation. Particularly, Leguizamón (2005) noted the potential to integrate *CA* models with data from *Digital Elevation Models* (*DEM*) and the like, thereby coupling to variables such as slope and insolation. Pardo-Igúzquiza et al. (2017) have subsequently deployed *CA* models to estimate *SCA* across an area of $2000\,km^2$ in the Sierra Nevada mountain range, calibrating and validating against *MODIS* $f_{SCA}$ (460 m resolution). Recent studies, though, call for caution in the use of *MODIS* for validating spatially distributed snow models, as it does not capture the spatial heterogeneity of snow cover induced by solar radiation (Bouamri et al. 2021). In a further *CA* study, Collados-Lara et al. (2021) have assessed the impact of climate change on *SCA*, again for the Sierra Nevada mountain range. Summarising, modelling *SCA* through *CA* models offer an attractive solution when satellite data are lacking, or when they have low resolution compared with the operational resolution required by hydrological models (Pardo-Igúzquiza et al. 2017).

The key objective of this paper is to develop a novel and calibrated stochastic *CA* model for the evolving *SCA* of some mountain catchment area. Specifically, we focus on the *fine spatial scale*, so that subtle spatial variation in the distribution of snow coverage can be captured by the model. This, in turn, will allow the model to be used to determine whether there are distinct drivers of snowmelt that play particularly crucial roles as the snow coverage evolves from fully snow covered to fully exposed. The strength of the *CA* approach lies within the simplicity of the underlying assumptions, in that we require just two easily-obtained inputs: the varying elevation across the terrain, and the varying incidence angle across the terrain. Yet, despite this simplicity, an impressive fit is obtained when calibrated against *SCA* estimates obtained from high-resolution satellite images (see Section 2 for more details).

The remainder of this paper is organised as follows. In the next section we describe the study site, the key data necessary to simulate and calibrate the model, explain the model and describe our simulation study. We describe the results, exploring the relative necessity of different mechanisms to describe the dynamics of snow melt at different stages of the process. We conclude with a discussion, speculating on the cause of discrepancies between model and imaging data and providing the direction for future investigations.

## 2. Methods

### *2.1. Test site and input data*

#### *2.1.1. Study site*

Dora del Nivolet is a 17 $km^2$ high-elevation Alpine catchment located within the Gran Paradiso National Park territory in the Valle d'Aosta Region (Italy) (Fig.1). Elevation ranges from 2390 to 3430 m a.s.l., with an average slope of $\sim 20°$. The left side of the Dora del Nivolet catchment is of mainly south-east aspect and the right side is predominantly north-west facing. This catchment presents a snow-dominated hydro-climatic regime: the surface is typically snow-covered for roughly 6 months per year, from mid-November to mid-May, while during the growing season the catchment surface transforms into a typical alpine meadow as snow cover decreases. Notable are the extreme winds to which the terrain is exposed; for example, in February 2022 wind velocities of over 200 km/h were measured at Gran Paradiso National Park. Average daily temperatures span from -15°C during mid-winter to 20°C during mid-summer. The geology of the area mainly consists of gneiss, with bedrock emerging at high elevations and the talus prevailing at medium elevations.

#### *2.1.2. Elevation*

Topographical factors play a key role during snow melt and it is possible to obtain a detailed morphological description of the catchment region, starting from a *Digital Terrain Model* (*DTM*). In this study we use a *DTM* with 10 m resolution, provided through the Valle d'Aosta Regional geoportal. A pre-processing algorithm is applied to fill *DTM* sinks, thus removing small imperfections in the input data (Planchon and Darboux 2002, Tarboton et al. 1991). We delineate the Dora del Nivolet catchment area through the `r.watershed` and the `r.water.outlet` routines in *QGIS* software. The catchment outlet point corresponds to the discharge gauging station installed in the main stream, called "Dora del Nivolet river". We use the catchment area for clipping the filled *DTM* and export the clipped raster in `.TIFF` format, generating the first input data (Fig. 1**b**) for the *CA* model described in Section 2.2. Elevation is a crucial factor during the snow melt process, since it is inversely correlated with air temperature. Thus, while temperature is not explicitly incorporated (e.g., Pardo-Igúzquiza et al. 2017) as a model input data, it indirectly enters via the dependence on elevation.

#### *2.1.3. Incidence Angle*

Geomorphological attributes (including slope and aspect) considerably impact on the energy reaching the snow-covered surface, through sunrays triggering the phase transition that initiates snowmelt (Abudu et al. 2016). We aggregate the effect of these attributes through calculating the so-called *incidence angle* ($I$), defined as the angle between the sun's ray and the normal to the surface. Incidence angle for our study area is calculated using the `r.sun.incidout` algorithm in *QGIS* software (Fig. 1**c**). Note that estimation of the incidence angle across some landscape requires four inputs: (i) a raster layer of elevation; (ii) a raster layer of aspect; (iii) a raster layer of slope; and, (iv) the *Day Of Year* (*DOY*) and the hour for which we want to calculate $I$. Inputs (ii) and (iii) are calculated using the `r.slope.aspect` routine in *QGIS* software. Regarding the *DOY*, we select 139 (corresponding to May $19^{\text{th}}$, 2018), representing the first date for which the fraction of snow coverage across the site is lower than 1 and, hence, suggesting the onset of snow melt. For the hour we select midday, given that it is the time of the day for which the vast majority of pixels will be reached by sun rays. Note that using a time of midday minimises the presence of shaded pixels; those few (39, $\sim 0.045\%$) shaded pixels are treated as pixels that do not (directly) receive solar energy (i.e. incidence angle $I = 90°$). This incidence angle is then used as a proxy for the amount of solar energy reaching the surface (see Section 2.2).

*2.1.4. Snow Cover masks*

Data describing snow coverage evolution can be obtained through consulting high time and spatial resolution satellite images. Here we use the *Sentinel-2 Level-2A (L2A)* dataset for extracting snow cover masks over a *Period Of Interest* (*POI*); our study takes this period as May $25^{\text{th}}$ 2018 to July $30^{\text{th}}$ 2018, due to the availability of 5 cloudless multi-spectral images representative of the phase-down of snow cover. Snowy pixels in images are classified through the commonly used *Normalised Difference Snow Index* (*NDSI*), defined as (Dozier 1989):

$$NDSI := \frac{R_{\text{green}} - R_{\text{SWIR}}}{R_{\text{green}} + R_{\text{SWIR}}},$$

where $R_{\text{green}}$ denotes the reflectance in the green band (Sentinel-2 band 3) and $R_{SWIR}$ denotes the shortwave infrared reflectance band (Sentinel-2 band 11). *L2A* data is of high quality, in which the effects of the atmosphere on the light reflected from the surface are corrected through an *Atmospheric Correction (AC)* algorithm (Richter and Schläpfer 2011), applied to the *Level-1C (L1C)* product. A number of recent papers have employed *L2A* products for calculating *NDSI* (for example, Gascoin et al. 2020, 2019). Moreover, Hofmeister et al. (2022) tested the utility of *AC* on snow detection with *Sentinel-2* and observed increased snow detection performance at higher elevations when using atmospherically corrected data. Further, Härer et al. (2018) noted that even if the *NDSI* is an index which reduces the dependence on atmospheric conditions, applying *AC* might be necessary. Thus, we have used here the *Sentinel-2 L2A* dataset for the *NDSI* calculation.

Standard practice for producing a snow cover mask is to consider all pixels with an *NDSI* value above a defined threshold. The commonly used threshold is 0.4 (Dozier 1989), but recent studies suggest that a location-dependent threshold can provide superior results for higher spatial resolutions (Salzano et al. 2021, Aalstad et al. 2020, Härer et al. 2018, Yin et al. 2013). Following manual calibration of the *NDSI* threshold, we observed that a value of 0.2 is more suitable for the study area considered here, since it allows a more accurate estimation of snow patches (see Fig. 8 in the Appendix). Fig. 8 indicates that while a decrease in the threshold from 0.4 or 0.2 may not lead to substantial differences, the underestimation of real snow cover area for a threshold of 0.4 is greater than that for 0.2, potentially resulting in greater error of the snow cover masks. Since these masks directly calibrate the model following the random parameter search algorithm, described in Section 2.3, we require them to be as precise as possible: consequently, we set a threshold of 0.2. Note that lower thresholds than this are excluded, as the Snow Detection algorithm of the *European Space Agency* (*ESA*) determines that pixels with an *NDSI* value below 0.2 have effectively zero snow probability.

We calculate the *NDSI* via the built-in function provided by the free web application *EO Browser*, powered by *Sentinel Hub* with contributions from the *ESA*. We select a sequence of five images (on dates with no cloud cover) over the *POI*, revealing a gradually decreasing snow cover percentage, see Fig. 1**d**. In broad terms, we note that the initial snow melt is concentrated to the north central region of the catchment area (highlighted region in May $25^{\text{th}}$ image of Fig. 1**d**). An uncovered tract emerges, predominantly expanding upslope in a southwesterly direction (arrows in June $14^{\text{th}}$ image of Fig. 1**d**). By late July, minimal levels of snow coverage remain, principally concentrated around regions of higher elevation. Snow cover masks are downloaded as georeferenced (WGS 84 - EPSG: 4326) `.TIFF` files, where each mask is characterised by 366x371 pixels with a latitude resolution of $\sim 0.00013$ deg/pixel and a longitude resolution of about $\sim 0.00018$ deg/pixel ($\sim 14 \times 14\,\text{m}^2$).

*2.2. Model design*

A stochastic cellular automaton has been built to simulate snow melt across the study site. The key steps considered during the design of the model were as follows:

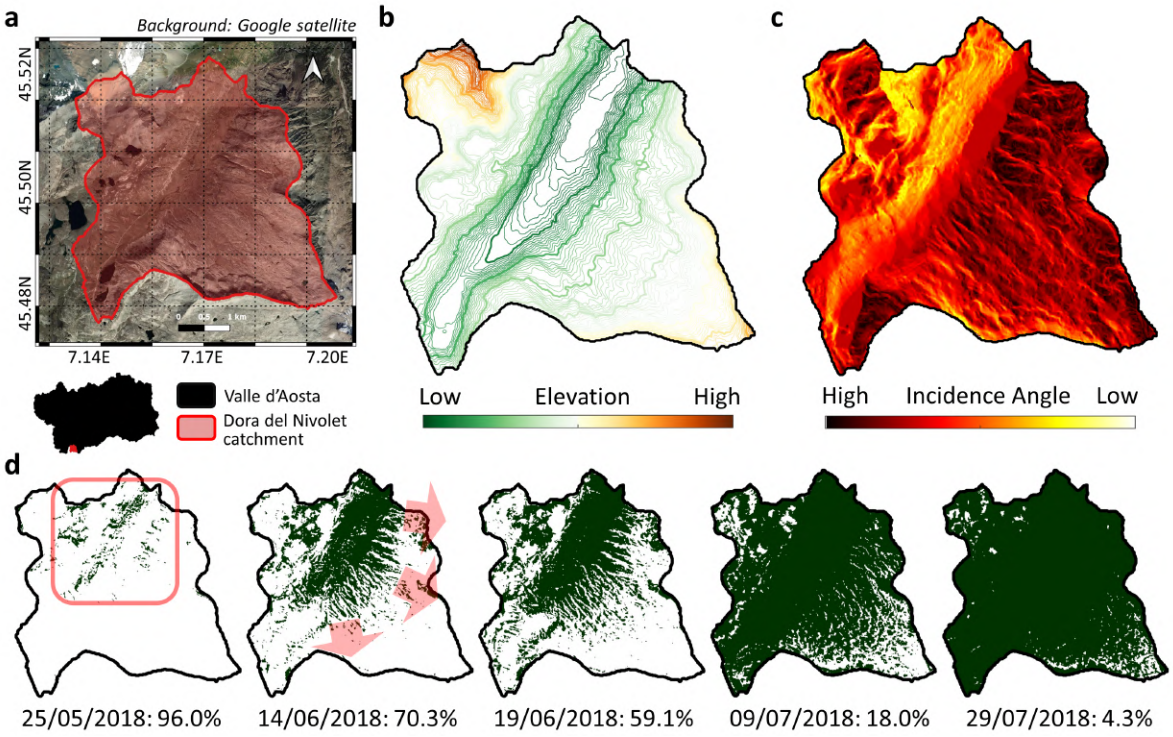


Figure 1: **a** Position and structure of the catchment area, Dora del Nivolet in the Valle d'Aosta region of north-west Italy. **b** Elevation profile of the catchment site, ranging from a low of 2,390m to 3,430m. **c** Incidence angle of the test site, calculated according to the terrain aspect and sun position at 12:00, May $19^{th}$ 2018. **d** Sequence showing the evolving snow coverage area, as estimated from remote sensing, across the period of interest (see Section 2.1.4). The remaining snow coverage within the catchment is indicated as a percentage, in terms of proportion of catchment area pixels still covered by snow.

i. Discretising the physical domain into a regular lattice of patches, where each represents a square portion of terrain (of dimensions $\Delta x \times \Delta x$);
ii. Designating the possible patch states (snow or grass);
iii. Defining an appropriate transition probability function $P(x, t)$, that determines the probability that a patch centred at $x$ transitions from one state to another between time $t$ and $t + \Delta t$;
iv. Incorporating the environmental dependencies into the transition probability function.

*i. Discretisation of the physical domain*

We design our model to describe snow coverage across a landscape surface or *domain*, $\Omega$. Our model takes the form of a stochastic cellular automaton, where the physical domain is discretised onto a simulation domain formed as a two dimensional regular lattice of non-overlapping and space-filling cells, called *patches*, see Fig. 2**a**. Specifically, the simulation domain is formed from the union of a set that contains a total of $N$ patches, where patch $i$ corresponds to a square portion of ground of dimensions $\Delta x \times \Delta x$ and centred at position $x_i$. Note that we will drop the subscript $i$ where it can be done so without ambiguity. Note further that the patch dimensions are according to the satellite-derived datasets of snow coverage described in the previous section. In other words, $\Delta x$ is the spatial scale of each pixel in a snow cover mask of the study region ($\Delta x \sim 14\,\mathrm{m}$).

*ii. Patch states*

Each patch is assigned a state that denotes whether the patch is covered by snow or bare ground (hereafter referred to as grass, though of course it could also be rock or lake surface etc). We

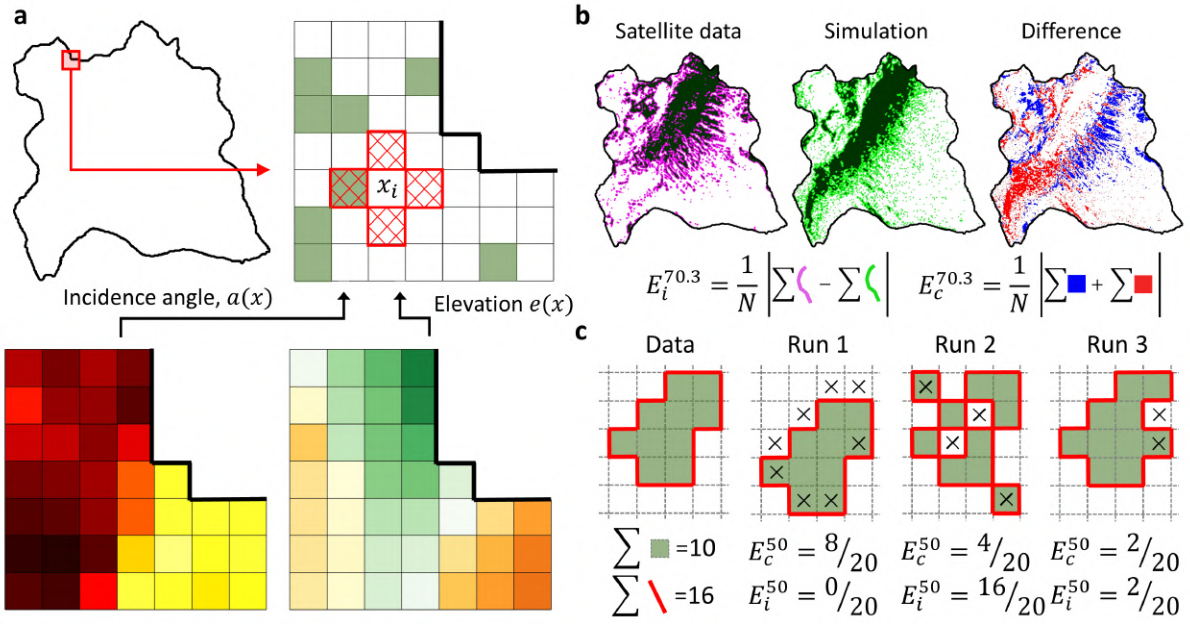


Figure 2: **a** Domain representation. The catchment region is discretised onto a regular square lattice, with each patch the dimension of a pixel from the satellite image data ($\sim 14 \times 14\,\mathrm{m}^2$). Patch state is binary: snow (white) or grass (green), with the transition dynamics governed by the state of the Neumann set of nearest neighbours (hatched red squares for the patch indicated $x_i$) and inputs based on elevation data and incidence angle data. **b** Measures used to fit the model against satellite image data. Satellite data and simulation outputs are compared at equivalent stages of remaining snow cover area (here, 70.3%). At each stage, the map of snow or grass cover (respectively, white or black pixels) is recorded, as is the length of the snow/grass interface (length of purple/green lines). The two measures are the interface-based error, $E_i$, and the coincidence-based error, $E_c$. The interface-based error is simply the absolute difference in interface length, normalised with respect to the total number of patches. The coincidence-based error is the sum of the (absolute) difference between patch states, again normalised with respect to the total number of patches. In the difference map, white pixels indicate match between satellite data and simulation, while red (blue) indicates snow (grass) in satellite data but grass (snow) in simulation. The coincidence error is hence based on the sum of blue and red pixels, divided by the total number of patches. **c** An explicit calculation of coincidence and interface errors, for a hypothetical satellite dataset and three separate runs of the simulation model. Green and white squares represent grass and snow, respectively, while red lines indicate the interface. Squares marked with crosses indicate a mismatch in the patch state. See text for details.

denote the state of a patch at $x$ at time $t$ by $S(x,t)$, where $S = 1$ represents snow coverage and $S = 0$ represents grass. This simplification to a square lattice of binary state patches facilitates a straightforward comparison with the satellite-imaged data where, as described above, each pixel can be attributed as snow or bare ground. At the start of each simulation we assume 100% snow coverage across the domain, $S(x_i, 0) = 1$ for $i = 1 \ldots N$. Since snow melting is an inherently stochastic process (e.g. local temperature fluctuations, shifting wind patterns *etc*), we model the transition from snow to grass at a patch as a Markov (i.e. memoryless) stochastic process. Note further that we do not allow the reverse process, i.e. from grass to snow. This, in effect, supposes a one-way process across a season in which fresh snowfall is either negligible or rapidly melts. The *CA* approach allows us to forsake a more physics-based description, permitting instead a phenomenological approach that facilitates straightforward simulation and calibration.

*iii. Snow to grass transition probability*

For a patch located at position $x$, the probability that it melts during the time interval $[t, t+\Delta t]$ is assumed to be

$$P(x,t) = e^{-\rho f(x,t)}\,, \tag{1}$$

ensuring $P(x,t)$ is bounded between 0 and 1 for $\rho \geq 0$ and $f(x,t) \geq 0$. The *melt likelihood parameter* $\rho$ is an independent parameter that sets the likelihood of snow melt occurring during

the time interval $[t, t+\Delta t]$, and we take this here to be a constant. Note that the exponential dependence generates multiple orders of variation in the probability of snow melt, allowing the different factors to have a potentially large impact on snow melt.

*iv. Transition dependencies*

The function $f(x,t)$ forms the focal point through which factors that influence snow melting can be introduced. As noted above (see Fig. 2**a**), here we consider a dependence on each of:

(i) *elevation,* $E$;
(ii) *sun incidence angle,* $I$;
(iii) *neighbourhood state,* $N$.

Dependence on the sun incidence angle accounts for the fact that terrain more heavily exposed to sun will receive greater energy. As described earlier, a patch at $x$ is associated with an angle $\Theta(x) \in [0°, 90°]$, where $\Theta(x) = 0°$ ($\Theta(x) = 90°$) indicates orthogonal (parallel) rays. This angle is straightforwardly rescaled onto a function $a(x) \in [0,1]$, where $a(x) = 1$ ($a(x) = 0$) indicates that the patch at $x$ receives maximum (minimal) direct energy.

Elevation is also expected to impact on the rate of snow melt, since higher terrain is linked to lower air temperatures and greater snowfall. Elevation is encoded into the model similar to incidence angle above, i.e. through a rescaled function $e(x) \in [0,1]$ in which a patch at $x$ satisfying $e(x) = 1$ ($e(x) = 0$) correspond to patches with lowest (highest) elevation across the domain.

Dependence on neighbour state introduces a source of nonlocality: snow melt in a patch could be more likely if surrounding patches have already melted. This could be derived from a similarity between neighbouring sites not explicitly included through dependence on elevation or aspect: for example, similar initial snow depth, microclimate, ground composition *etc.* It could also be viewed in the light of local heat transfer, where the lower reflectance of grass compared to snow will lead to the absorption of more solar energy in the neighbourhood, if surrounding patches have already melted. Without specifying the precise source of this neighbourhood dependence, for each patch $i$ we keep track of the (time-dependent) proportion of grass covered neighbours. Letting $\mathcal{N}_i$ denote the set of neighbouring patches (and $|\mathcal{N}_i|$ the number of neighbouring patches) with respect to the patch indexed by $i$, the proportion of grass-covered neighbours for patch $i$ will be

$$b(x_i,t) = 1 - \sum_{j\in\mathcal{N}_i} \frac{1}{|\mathcal{N}_i|} S(x_j,t)\,.$$

Note that the set of neighbours is based (for an internal patch) on the 4 nearest neighbours, i.e. according to a von Neumann neighbourhood (e.g. see Ghosh et al. 2017).

Summarising, $a(x)$, $e(x)$ and $b(x,t)$ are functions bounded between 0 and 1 and provide measures for the incidence angle, elevation and neighbourhood state, respectively, for a patch at position $x$ and time $t$. We amalgamate these into a governing function, $f$:

$$f(x,t) = \frac{(1+\alpha^p \bar{a}^p)(1+\beta^q \bar{e}^q)}{(1+\alpha^p a(x)^p)(1+\beta^q e(x)^q)(1+\gamma^r b(x,t)^r)}\,. \tag{2}$$

The *weighting parameters* $\alpha$, $\beta$ and $\gamma$ are dimensionless and non-negative, their sizes reflecting the influence of incidence angle, elevation and neighbourhood state on snow melt, respectively. Regarding the *nonlinearity parameters* $p$, $q$ and $r$, we consider two model formulations. The *basic* model simply assumes $p = q = r = 1$, a linear relationship which minimises the fitting to just 4 parameters (the weighting parameters, along with the independent parameter $\rho$). We also consider an *extended* formulation, where $p, q, r$ can also be varied to provide greater subtlety in the calibration.

Note that $\overline{a} = \frac{1}{N}\sum_{i=1}^{N} a(x_i)$ and $\overline{e} = \frac{1}{N}\sum_{i=1}^{N} e(x_i)$ denote the mean incidence angle and mean elevation averaged across the domain, respectively. The factor in the numerator of Eq. (2) is therefore a normalisation, so that $f(x,t) = 1$ for an *average patch* at $t = 0$, irrespective of $(\alpha, \beta, \gamma)$. An average patch at $t = 0$ refers to a patch with incidence angle and elevation at the mean values, and with only snow-covered neighbours: i.e. $a(x) = \bar{a}, e(x) = \bar{e}, b(x,0) = 0$. We note further that $f(x,t)$ is decreasing with respect to each of $a, b$ and $e$ and will therefore be maximum for a patch satisfying $(a(x), e(x), b(x,t)) = (0,0,0)$ (no direct sun, highest altitude and snow-covered neighbours) and minimum for a patch satisfying $(a(x), e(x), b(x,t)) = (1,1,1)$ (fully exposed, lowest altitude and grass-covered neighbours). Given the decreasing dependence on $f$ in Eq. (1), snow melt in a given timestep is then least likely (most likely) for the former (latter).

The numerical simulation algorithm for simulating the model was implemented in MATLAB© and is described in Appendix C. We note that the code (along with necessary inputs) has also been made available to download at `https://github.com/kjpainter/SnowMeltNivolet`.

### *2.3. Model analysis and fitting*

Overall the model requires a set of fixed inputs obtained from data (elevation and incidence angle of each patch, geometry of the domain), along with a set of governing parameters. The parameters fall into two principal classes: those describing discretisation of space and time ($\Delta x$, $\Delta t$), and those that govern the probability of snow melt in a patch $(\rho, \alpha, \beta, \gamma, p, q, r)$.

In terms of discretisation parameters, $\Delta x$ corresponds to the resolution of snow cover masks (here, $\Delta x \sim 14$m). For $\Delta t$ we assume this to be dimensionless in the present study. This exclusion of explicit time is a simplification that allows us to focus on the spatial pattern of snowmelt – e.g. where melt occurs at different stages – rather than the snowmelt rate. This in turn simplifies the model fitting (described below). In the discussion we provide further commentary on this point.

Appropriate parameters $(\rho, \alpha, \beta, \gamma, p, q, r)$ will vary according to the geographical and geomorphological features of the study site. The phenomenological nature of the model precludes direct estimates of these from observations, and it is probable that there is no unique optimal parameter set (i.e. parameters that give a globally best fit against the estimated snow cover masks). Therefore, our analytical approach here will be to assess the *goodness of fit* across a spectrum of models of increasing complexity, through adopting a randomised parameter search and trial process. Specifically, we proceed as follows:

i. Classify the models to be tested, through designating a region of $(\rho, \alpha, \beta, \gamma, p, q, r)$ parameter space to explore;
ii. Randomly sample parameter space to generate a set of parameter combinations to test;
iii. Perform simulations at each parameter combination in the set, recording information on the evolving snow/grass distribution;
iv. Assess the *goodness of fit* for a particular parameter combination though comparing simulation data against the coverage estimated from satellite-derived snow masks.
v. Assess the goodness of fit of a particular model through evaluating performance across top-ranking parameter combinations.

#### *i. Sequence of models to be tested*

The initial aim is to explore which of the considered dependencies allow for better or worse recapitulation of the snow melt distribution estimated from remote sensing. To this end, the first study will focus on a basic model scenario ($p, q, r$ fixed such that $p = q = r = 1$), in which we systematically explore eight sub-models of varying level of complexity. These are as follows:

- The null model, *0-model*, where none of the dependencies are incorporated. This serves as a baseline case for reference.

| Parameter | Basic Null | Basic I | Basic E | Basic N | Basic IE | Basic IN | Basic EN | Basic IEN | Extended IEN |
|---|---|---|---|---|---|---|---|---|---|
| $\rho$ | $[2, 10]$ | $[2, 10]$ | $[2, 10]$ | $[2, 10]$ | $[2, 10]$ | $[2, 10]$ | $[2, 10]$ | $[2, 10]$ | $[2, 10]$ |
| $\alpha$ | 0 | $(0, 9]$ | 0 | 0 | $(0, 9]$ | $(0, 9]$ | 0 | $(0, 9]$ | $(0, 9]$ |
| $\beta$ | 0 | 0 | $(0, 9]$ | 0 | $(0, 9]$ | 0 | $(0, 9]$ | $(0, 9]$ | $(0, 9]$ |
| $\gamma$ | 0 | 0 | 0 | $(0, 9]$ | 0 | $(0, 9]$ | $(0, 9]$ | $(0, 9]$ | $(0, 9]$ |
| $p, q, r$ | 1 | 1 | 1 | 1 | 1 | 1 | 1 | 1 | $[0, 3]$ |

Table 1: Parameter ranges for the random sampling of parameter space and the fitting against satellite-based estimates of snow coverage. The snowmelt likelihood parameter $\rho$ is varied in all models. Parameters $\alpha, \beta, \gamma$ define the weighting of the dependency on incidence angle, elevation or neighbouring state, respectively; setting any of these to zero effectively removes that dependency from modelling of snowmelt, generating a sequence of submodels. The nonlinear parameters $p, q, r$ are set to 1 within the basic models, but allowed to vary for the extended model and hence provide further refinement to the fitting procedure.

- Single-layer models, *I-,E-,N- models*, where only one of incidence angle *(I)*, exposure *(E)* or neighbour *(N)* dependency is included
- Double-layer models, *IE-, IN-, EN-models*, where two of incidence angle, exposure and neighbour dependency are included.
- A triple-layer model, *IEN-model*, where all three dependencies are included.

Each model is implemented by setting the permissible range of the relevant weighting parameter. For example, for the null model the only parameter allowed to vary is the snowmelt likelihood parameter $\rho$, with each of the dependency weighting parameters $\alpha, \beta, \gamma$ set to zero. For the IN-model, on the other hand, each of $\rho$, $\alpha$ and $\gamma$ are positive, with only $\beta$ set to zero. The second study will then compare the basic *IEN-model* with an extended *IEN-model*, where in the latter case the parameters $p, q$ and $r$ are allowed to vary. Summarising, each of the models to be tested corresponds to exploring a particular regime of the $(\rho, \alpha, \beta, \gamma, p, q, r)$ parameter space.

In the absence of observations that can set parameter values, we set ranges for each of the parameters that will allow both a broad region of parameter space to be explored, while also allowing simulations to be performed within computationally reasonable times. Note that the adoption of the exponentially decaying form (1) already allows probabilities to vary across numerous orders of magnitude as certain parameters are altered. The choice of $\rho$ determines the probability of snow melt in a single timestep for an average patch at the start of snow melt ($t = 0$). Setting $\rho \in [2, 10]$ allows this probability to vary between $O(10^{-1})$ and $O(10^{-5})$: probabilities much higher than $\sim 10^{-1}$ will lead to almost immediate snow melt across the entire domain (unrealistic), while probabilities below $\sim 10^{-5}$ demand exorbitant computation time (unfeasible).

Parameters $\alpha, \beta, \gamma$, when "switched on", are set at $(0, 9)$. These ranges allow each mechanism to generate a tenfold variation in the size of $f$, and (given the exponential form) even larger variation in the size of the probability (1). Under the extended formulation we assume $p, q, r$ can take on values between 0 and 3. The sub-models and permitted parameter ranges are summarised in Table 1.

*ii. Parameter space sampling*

For each model listed in Table 1, simulations are conducted at given $(\rho, \alpha, \beta, \gamma, p, q, r)$ parameter combinations. First, 5000 parameter combinations are randomly generated through sampling from the relevant region of parameter space. To establish a relatively even distribution of sample points within the parameter space, a Latin Hypercube Scheme is adopted (McKay et al. 1979); operationally, we adopt the `lhsdesign` routine in MATLAB©. We note that the density at which the parameter space is sampled will depend on the dimensionality of the parameter space:

thus, for example, the parameter space of the triple layer model is sampled at a lower density than each of the double layer models. Nevertheless, we sample the same number of parameter combinations for each model, so that statistics are compared across an equivalent number of simulations.

*iii. Simulation protocol*

The stochastic nature of the model means that the precise output will vary with each simulation, even under the same inputs. Consequently, for each model at each parameter combination, 5 simulations are performed and the results are averaged. Note that exploratory analyses demonstrated that the fit under a particular parameter combination would vary minimally across these 5 simulations (for example, see Appendix D), hence this number was deemed an acceptable compromise between accuracy and computational cost. Overall, with the number of models (9), the number of tested parameter combinations for each model (5000) and the number of simulations for each parameter combination (5), more than 200000 simulations of the model were performed for the analysis presented here. We note that the results of an analysis with fewer parameter combinations (1000) and fewer simulations per parameter combination (3) gave qualitatively similar behaviour, suggesting that our exploration was sufficiently deep to generate meaningful conclusions.

*iv. Error measures and goodness of fit*

To assess the goodness of fit for a particular model at a particular parameter combination, it is necessary to specify *error functions* that compare simulation output with the satellite derived *SCA* estimates. Let $S_{si}^{z\%}(x_i)$ denote the snow coverage (1 = snow, 0 = grass) from satellite image masks (see Section 2.1.4) at pixel or patch $x_i$, when snow coverage is at $z\%$ of the domain. The corresponding snow coverage from the stochastic simulation model at $x_i$ is recorded at the equivalent stage of domain coverage, and denoted by $S_{ss}^{z\%}(x_i)$.

We consider two error measures, based on the *spatial coincidence* and the *snow-grass interface*, see Fig. 2**b**. Spatial coincidence is simply the mean of the absolute difference between satellite image and simulation output. For a satellite image indicating $z\%$ coverage, we set

$$E_c^{z\%} = \frac{1}{N}\sum_{i=1}^{N}\left|S_{si}^{z\%}(x_i) - S_{ss}^{z\%}(x_i)\right| \tag{3}$$

A value $E_c^{z\%} = 0$ indicates perfect match between the satellite image and the model at $z\%$ snow coverage. For the interface error we first compute the total length of the interface between snow and grass patches/pixels, denoting these lengths by $L_{si}^{z\%}$ and $L_{ss}^{z\%}$ for the satellite image and stochastic simulation at $z\%$ coverage, respectively. The error based on interface length is then computed as

$$E_i^{z\%} = \frac{1}{N}\left|L_{si}^{z\%} - L_{ss}^{z\%}\right| . \tag{4}$$

Again $E_i^{z\%} = 0$ indicates that the snow/grass interfaces calculated for the satellite image and simulation output are of the same length at $z\% = 0$, although we note that this could occur even if $E_c^{z\%} > 0$. The two errors are combined into an amalgamated error function

$$E = \frac{1}{|\mathcal{Z}|}\sum_{z\in\mathcal{Z}} \lambda E_c^{z\%} + (1-\lambda)E_i^{z\%} . \tag{5}$$

The parameter $0 \leq \lambda \leq 1$ weighs the relative contribution of coincidence and interface errors: note that the majority of the analysis/presentation of the results is according to the value $\lambda = 0.75$ (default), but results are also presented for $\lambda = 1$ and $\lambda = 0$. The rationale for the default value is included in the Results below, with more detail in Appendix D. $\mathcal{Z}$ denotes the set of masks used in the calibration of the model to satellite imaging data, while $|\mathcal{Z}|$ denotes

the number of elements in this set. Note that the majority of the analysis will be based on calibration against all available snow cover masks, for our case study

$$\mathcal{Z} = \{96.0\%, 70.3\%, 59.1\%, 18.0\%, 4.3\%\} \ . \tag{6}$$

Calibrations will also be performed against a single snow cover mask, for example choosing $\mathcal{Z} = \{59.1\%\}$ if collaborating against the estimated snow melt near the middle of the *POI*.

Note that the rationale for an overall error that combines coincidence and interface match is illustrated through the hypothetical scenario shown in Fig. 2**c**. Coincidence is the obvious measure, yet relying solely on this can be flawed, as shown by comparing runs 1 and 2. While run 1 displays an identical snow melt *shape*, displacement in the shape leads to poorer coincidence than the speckled output from run 2. The additional comparison of interface length introduces a cost to significantly distinct shapes. A more optimal output may be of the form of run 3, where neither coincidence nor interface error is excessively high.

Coincidence and interface error measures, Eqs. (3) and (4), are calculated for each simulation and at each stage of snow melt using in the fitting, i.e. based on the choice of $\mathcal{Z}$.

*v. Ranking of parameter sets and models*

Given a value of $\lambda$ and the specification of $\mathcal{Z}$, for each simulation of the model Eq. (5) can be calculated. To obtain the goodness of fit under a certain parameter combination, the error Eq. (5) is then averaged across the 5 simulations. Following the full set of simulations over 5000 parameter combinations for a model, the parameter combinations are ranked from lowest (i.e. best fitting) to highest (i.e. worst fitting) error. Inevitably, many of the (randomly sampled) combinations originate from regions of parameter space that generate a poor fit with respect to the estimated *SCA* masks. Consequently, a model's capacity to fit data is examined based on its performance within the 1% top-ranked parameter combinations. Errors (e.g. see Appendix D) are noted to deviate only within a few percent across these 1% parameter combinations, while it also ensures enough combinations are used within the analysis to avoid the issues of sensitivity that could arise when a specific parameter combination is used. Note that results when using the top 0.5% or top 2% were qualitatively equivalent.

## 3. Results

### *3.1. Fitting of the basic model*

The null model excludes dependence on incidence angle, elevation or the neighbourhood, i.e. an environment of uniform elevation and independent patches. Hence, the mean number of time steps until a given patch transitions into grass varies only with $\rho$. Snow melt in the null model (representative simulation in Fig. 4**a**) is characterised by a random transition to grass in "salt and pepper" fashion, and (unsurprisingly) a poor fit against satellite data. Therefore, we adopt this as the baseline and errors for the various models analysed are reported in terms of improvement over the null model.

We explore how the different factors contribute to distinct snow melt characteristics. To this end, we compare the models based on a ranking according to only coincidence-based error ($\lambda = 1$) or only interface-based error ($\lambda = 0$). Results are presented in Fig. 3 **a,b**. Overall, incorporation of elevation data leads to the best spatial correlation between satellite-derived snow masks and simulation (top four models all include elevation data, Fig. 3**a**), while dependence on neighbourhood state leads to the best interface-based error (top four models all incorporate neighbourhood dependence, Fig. 3**b**). Directly examining simulation output offers further insight and, to aid explanation, a set of representative simulations for each single layer model is included in Fig. 4.

Incorporating elevation and/or incidence angle data biases melt towards particular regions, Fig. 4**b,c**. Incidence angle concentrates the initial snow melt north-west of the Dora del Nivolet

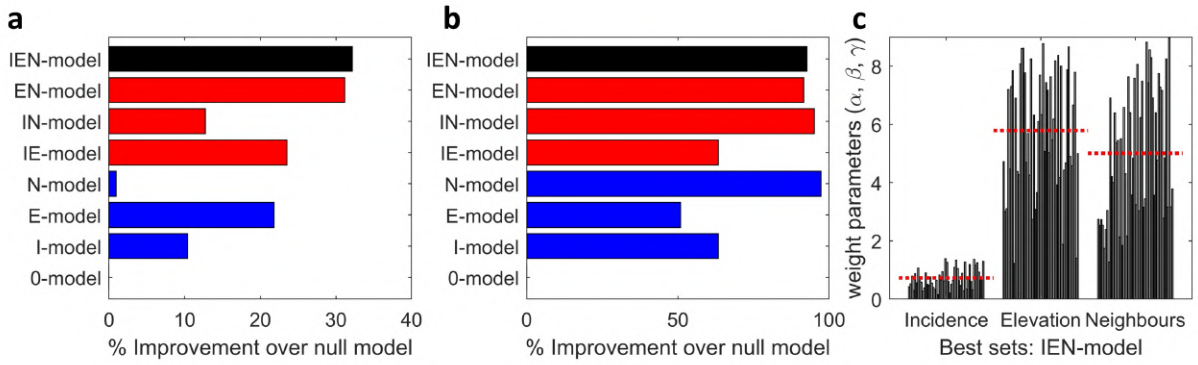


Figure 3: **a** Coincident-based and **b** Interface-based error improvement for each model, with respect to the null model. Specifically, we compute the mean error across the top 1% ranked parameter sets in each model class, following the sampling of the parameter space. In **a** the ranking is according to Eq. (5) with $\lambda = 1$, while in **b** $\lambda = 0$. **c** Values of the weighting parameters $(\alpha, \beta, \gamma)$ in the top 1% ranked parameter sets for the IEN-model, based on $\lambda = 0.75$ in Eq. (5). The dashed-red lines indicate the mean values for each of $\alpha$ (aspect), $\beta$ (elevation) and $\gamma$ (neighbourhood). Note that for all simulations, calibration is against all available snow cover masks, i.e. $\mathcal{Z}$ is given by Eq. (6).

valley, along with other terrain with a sun-facing aspect. Elevation, meanwhile, concentrates snowmelt along the lower altitude valley along which the stream runs. These regions are broadly consistent with early snow melt observed in satellite images, yielding reasonable coincidence-based error. However, incidence angle or elevation on their own will continue to result in a highly speckled pattern, as melting at one site has no direct impact on melting at neighbouring patches. This lies in contrast to satellite images, where initial points of snow melt expand to form large tracts of uncovered ground. Speckling manifests in a higher snow-grass interface, compared to satellite data, and consequently poor error when the interface-based measure is taken into consideration.

Dependence on the neighbourhood explicitly assumes a greater likelihood of melt if neighbouring patches have melted. This leads to points of melt that expand and fuse, Fig. 4**d**, and this patch to patch linking of snowmelt can dramatically improve the interface error; for example, we observe a close to 100% improvement against the null model, Fig. 3**b**. However, in the absence of a localising bias this occurs uniformly across the domain and a poor coincidence-based error results when only neighbourhood dependence is incorporated. Consequently, an error that balances the two measures is needed to derive suitable parameter sets. For the remaining analyses we use the default $\lambda = 0.75$ in Eq. (5), see Appendix D for full details.

Representative simulations of best-fit parameter sets for each double layer model and the triple layer model are provided in Fig. 5. The combination of neighbourhood and at least one of elevation or incidence angle allows plausible calibration of the model against data, Fig. 5**b-d**: elevation and/or incidence angle provides the initial localising bias, with neighbourhood dependence expanding melt into spatially extended tracts of exposed ground. Excluding a neighbourhood effect, though, continues to generate speckling, Fig. 5**a**, and hence less improvement with respect to interface error.

The best-fitting model is the IEN-model, to be expected given that other models arise as a limiting case (e.g. the EN-model arises as $\alpha$ approaches zero). More surprising, though, is the relatively small difference between the EN-model and IEN-model: compare the similar snow melt pattern in Fig. 5**c,d** and the minimal difference in errors (Fig. 3**a,b**). Examining the weighting parameters $(\alpha, \beta, \gamma)$ in the basic IEN-model across the top 1% parameter sets, Fig. 3**c**, the mean of $\alpha$ (incidence angle) across best matching sets is significantly smaller than those of $\beta$ and $\gamma$ (elevation, neighbours). Thus, excluding incidence angle (setting $\alpha = 0$) has a relatively small impact on the pattern of snow melt. This suggests that a reasonable "minimal model"

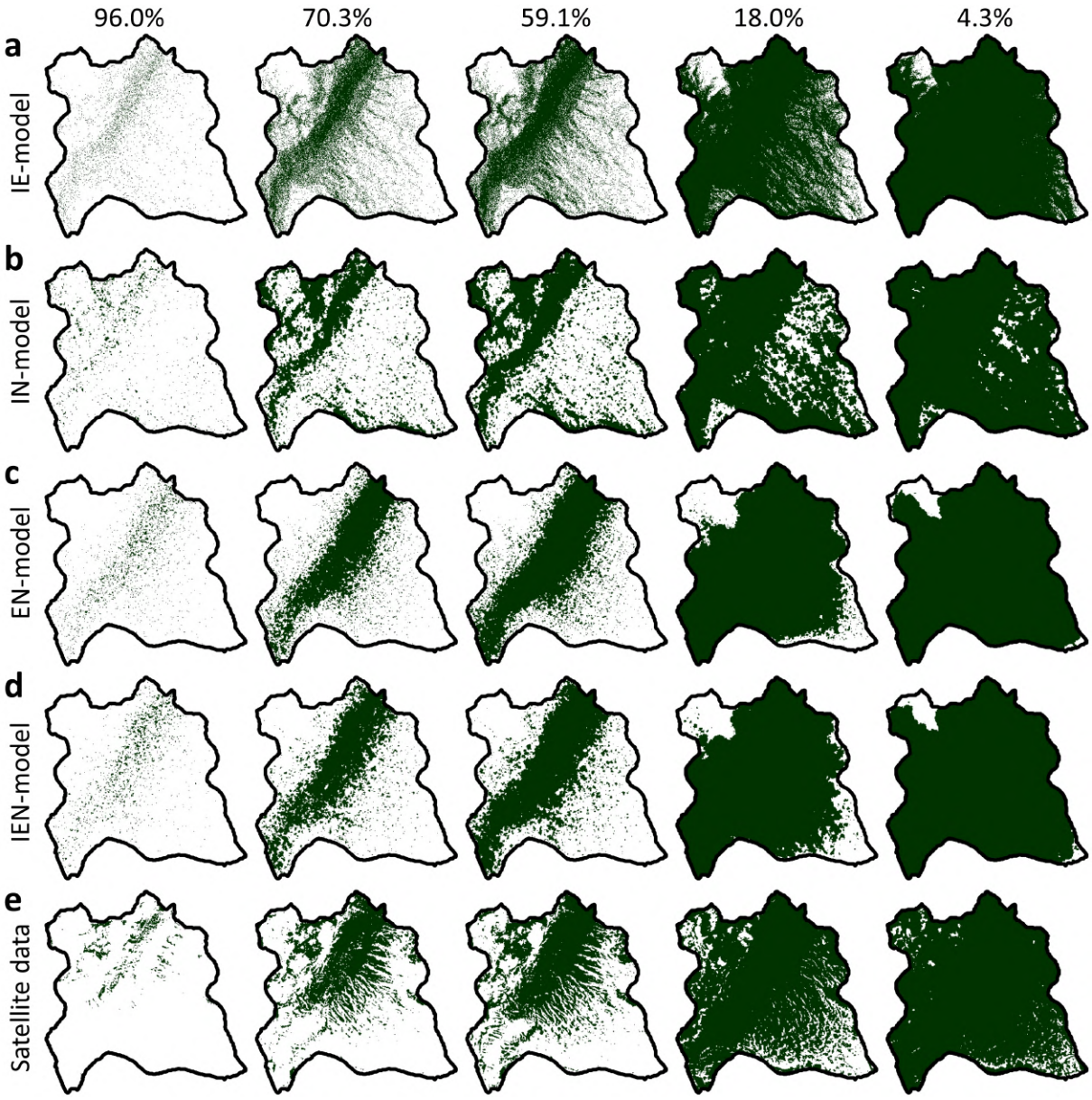


Figure 4: Representative simulations of the "best-fit" parameter set solution for the null and single layer models. For each model class, the best-fit parameter set was selected as the top-ranked set following the parameter space sampling and calibration against satellite data, according to the mean of the errors (Eq. (5)) when averaged over 5 simulations for each tested parameter set, using $\lambda = 0.75$ and calibrating against all snow cover masks, Eq. (6).

for snow melt could perhaps be limited to just neighbourhood and elevation dependence. We note further that the top 1% parameter sets for the basic IEN-model demonstrate reasonable fluctuation about the mean values of each of $\alpha, \beta, \gamma$, despite the overall fit/error being similar. This suggests that the model is not sensitive to the precise choices of the parameters, rather it is the relative values of these parameters with respect to each other that is of importance.

### *3.2. Fitting against single snow cover masks*

The analysis above followed a calibration against all satellite snow cover masks (for our case study, a total of 5). This is logical in the context of capturing spatial snow melt across a season, but may also generate certain biases. Data is only available when cloud cover is negligible, leading to a nonuniform distribution of masks across time. For instance, we have two relatively close datasets (70.4% and 59.1% coverage, 5 days apart) followed by one at 18.1% coverage

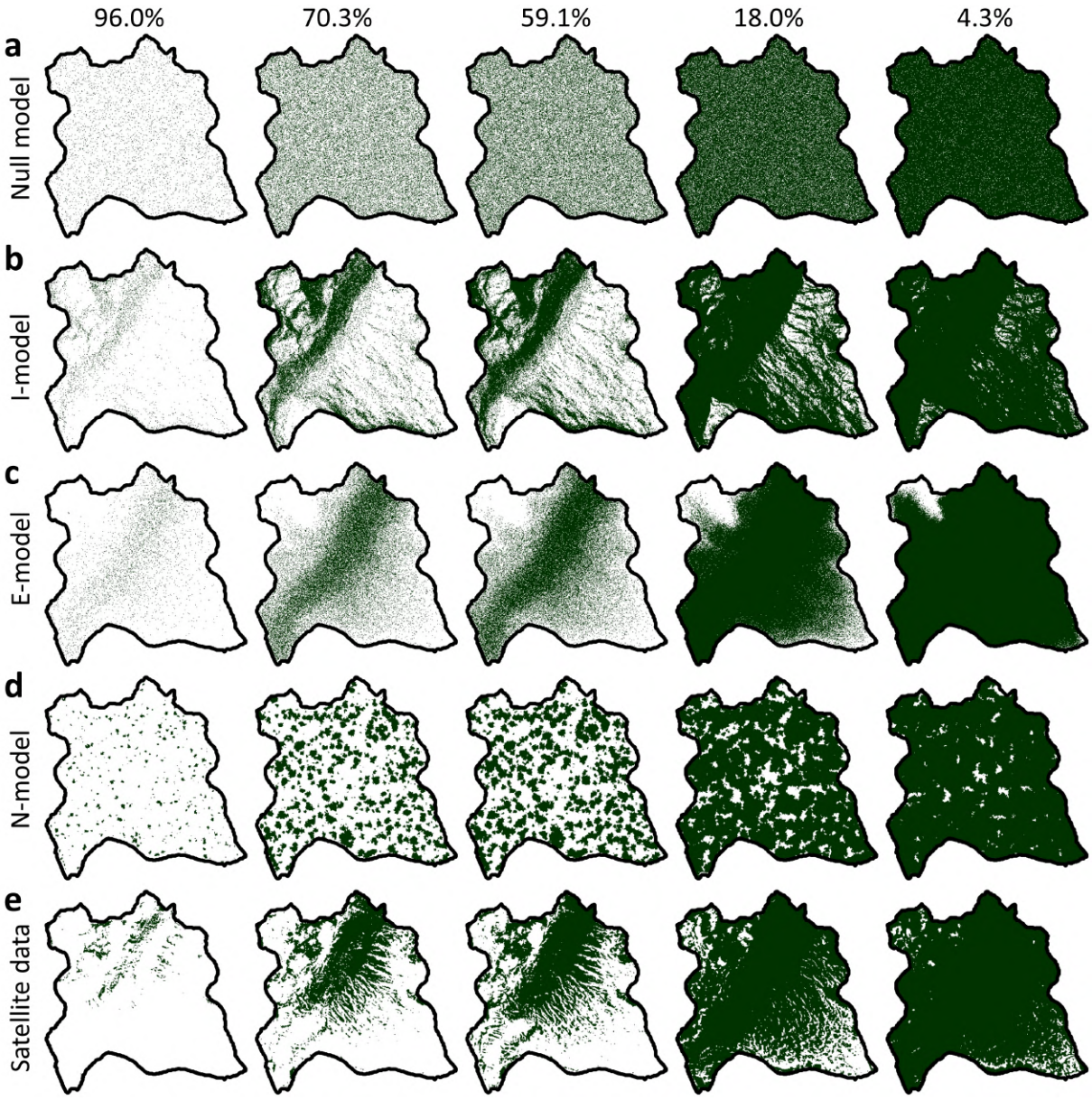


Figure 5: Representative simulations of the "best-fit" parameter set solution for the double and triple layer models. For each model class, the best-fit parameter set was selected as the top-ranked set following the parameter space sampling and calibration against satellite data, according to the mean of the errors (Eq. (5)) when averaged over 5 simulations for each tested parameter set, using $\lambda = 0.75$ and calibrating against all snow cover masks, Eq. (6).

(20 days later). Further, calibrating against all datasets across the period of interest implicitly assumes that the weighting of the individual contributing factors remains constant throughout snowmelt.

To understand the impact of these assumptions, we perform a series of calibrations against a single snow cover mask, e.g. setting $\mathcal{Z} = \{96\%\}$ in Eq. (5). In this way, we examine whether better fitting is possible when the strength of different influences is allowed to change across the course of the season. Fig. 6 synthesises the results of the analysis.

Notably, optimising the model against the earliest available snow cover mask (96.0% coverage) significantly increases the weighting with respect to incidence angle, Fig. 6**a**. Typical model output when calibrated at this early stage leads to a more spatially restricted snowmelt, concentrated in the upper central region and broadly consistent with satellite data. Optimising the model against mid-POI satellite images leads to weighting parameters dominated by elevation

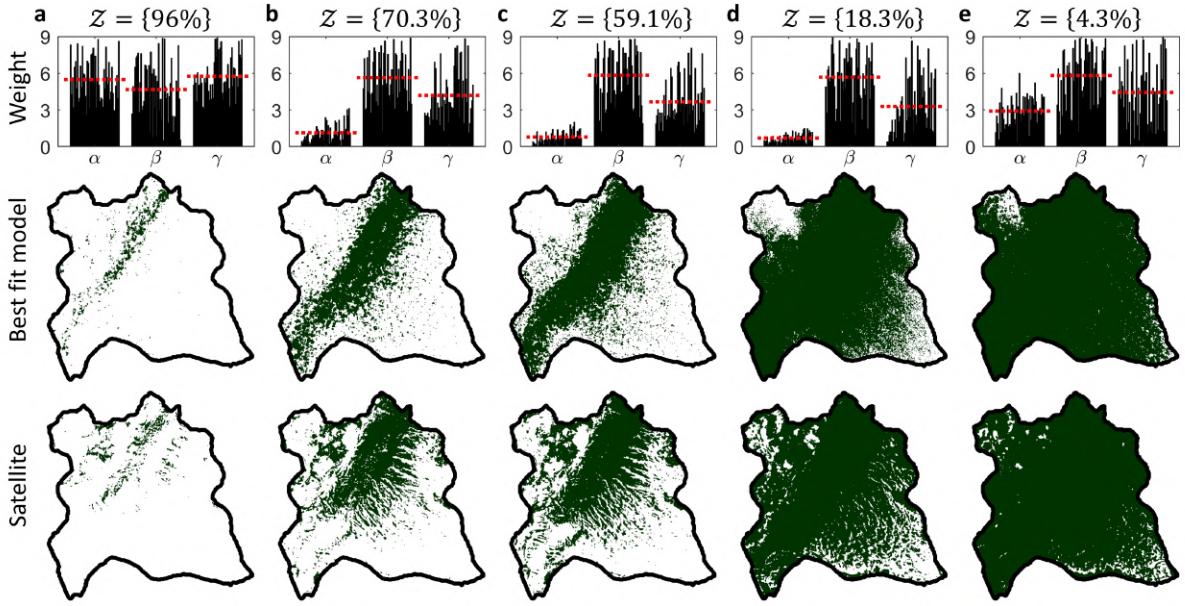


Figure 6: Fitting of the basic IEN-model against single snow cover masks, where **a** $\mathcal{Z} = \{96.0\%\}$, **b** $\mathcal{Z} = \{70.3\%\}$, **c** $\mathcal{Z} = \{59.1\%\}$, **d** $\mathcal{Z} = \{18.0\%\}$, **e** $\mathcal{Z} = \{4.3\%\}$. Top row shows the weighting parameters in the top 1% ranked sets (according to Eq. (5) with $\lambda = 0.75$), where the dashed red line shows the mean. Second row shows a representative simulation for the best fit parameter set, at the relevant stage of remaining snow cover. Third row shows the corresponding snow cover predicted from satellite data.

and neighbourhood, with results very similar to those when calibrating against the full set of snow cover masks. This reflects the greater data available within this period. When it comes to optimising against the latest stage of snowmelt, however, we once again observe a greater weighting for incidence angle.

Summarising, fitting against single satellite images suggests that an optimal model (and future extension of the framework) could include temporal variation across the course of the season, in terms of the influence of the different factors, whereby incidence angle becomes more significant during early and late stages of snow melt.

### *3.3. Fitting of the extended model*

The above analysis concentrated on the basic framework, i.e. Eq. (2) with $p = q = r = 1$. With a maximum of 4 parameters in the fitting, this allowed (relatively) fine scale exploration of the parameter space, but may also limit the degree to which the various controlling factors could influence snowmelt. Under the extended form, greater subtlety can be obtained (see Fig. 11 in the Appendix). Briefly, altering $p$ and $q$ concentrates or disperses the spatial heterogeneity generated from incidence angle and elevation, while changing $r$ alters the characteristic scale of melted tracts that spread from initial points of melt.

We analyse whether the extended model provides benefit in terms of calibration, now also allowing each of $p, q$ and $r$ to range between 0 and 3 when it comes to the random sampling of parameter space, in addition to the earlier ranges for $(\rho, \alpha, \beta, \gamma)$ (see Table 1). The basic model is a subclass of the extended model, so it is natural to expect the extended form to perform as well or better, *in the idealised case of full parameter space exploration.* However, given that the extended model contains almost twice the number of parameters to fit (7 against 4), sampling of parameter space for the same number of parameter sets (near equivalent computational cost) results in sparser exploration and uncertain benefit gain.

Results and typical simulations are presented in Fig. 7**a**. Comparing errors for the top 1% fitting sets in the extended-IEN model, against those in the basic model counterpart, we find significant

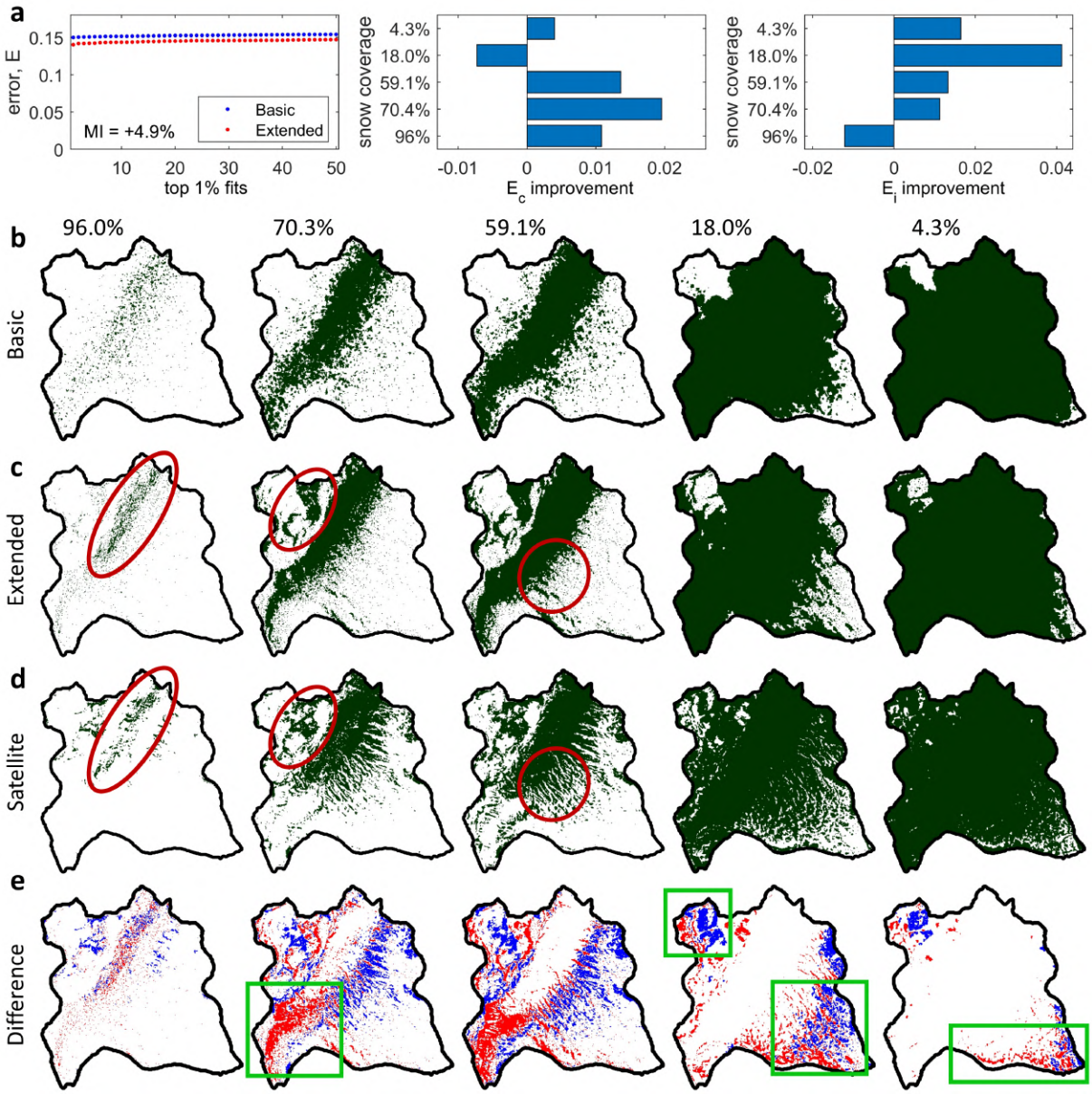


Figure 7: Fitting of the extended model. **a** Statistics following a 5000 set sampling of the parameter space, comparing the extended IEN-model against its basic counterpart. Ranking (using all available snow masks and $\lambda = 0.75$ in Eq. (5)) the top 1% parameter sets, the extended model consistently outperforms the basic model with an almost 5% error improvement. Comparing the best fitting set for each of the extended and basic model, coincidence and interface errors are near-universally improved across all stages of snow melt. **b** Representative simulation using the best-fit parameter set for the basic model; **c** Representative simulation using the best-fit parameter set for the extended model; **d** Snow cover masks from satellite images; **e** Difference between extended model and SI data, where red (blue) pixels indicate melt in the extended model (SI), but not in the SI (model), while white pixels indicate a match. A video showing the spatial evolution of snow melt is included in the Supplementary Information and made available at `https://youtu.be/M5FwGGA-2cE`

gain from using the extended model: an almost 5% error improvement across the top 1% fitting sets, Fig. 7**a** (left panel). Furthermore, when comparing coincidence and interface errors at various stages of snowmelt, the top ranking parameter set in the extended model showed near universal improvement in coincidence and interface match, Fig. 7**a** (middle and right panel).

To analyse how this improvement manifests itself at the spatial level, in Fig. 7**b-e** we compare representative simulations from the extended and basic model, under 'best-fit' parameter sets, against satellite snow cover masks. In particular, the extended model is found to replicate

subtleties observed in the satellite derived images. For example, we observe that snow melt becomes more concentrated to the upper middle portion of the domain during early snow melt (ellipses at 96.0%), earlier snow melt on the south slope in the northwest high elevation terrain (ellipses at 70.3%), and more clearly defined stripes extending southwesterly (circles at 59.1%).

Nevertheless, some notable discrepancies remain and we highlight these via the difference map (Fig. **7e**). Most prominently, our model consistently overestimates snow melt rate within the south eastern corner (square at 70.3%). Another notable discrepancy lies in the distinct snowmelt in the southwest (southwest square region at 18.0%), where while the model predicts "fingers of melt" that extend southeast, satellite data indicates stripes that curve into a southwest to northeast orientation. Furthermore, our model underestimates the snow melt in the high altitude northwest corner (square at 18.0%), but overestimates the melt occurring along the southern boundary (rectangle at 4.3%). Potential explanations for some of these discrepancies are discussed below.

## 4. Discussion

Monitoring snow cover is crucial for understanding the hydrology of mountain environments (Largeron et al. 2020), with the snow pack constituting a precious water source that demands carefully management (*SDG6*). Satellite images can provide only instantaneous snapshots of snow cover and clouds frequently obscure detail. As such, there exists an information gap that could be filled by a predictive model, sufficiently refined to predict evolving snow coverage at the operational resolution required by hydrological models (Pardo-Igúzquiza et al. 2017). In this study, we have developed a fine-scale stochastic cellular automaton model that describes how the spatial pattern of snow cover evolves across a mountain catchment. Notably, our case study represents a somewhat extreme example: an elevation gain of more than 1000 metres across the catchment, complex topography, exposure to extreme climatic conditions (Gisolo et al. 2022).

An advantage of the model lies in its formulation, requiring just two easily available spatial inputs: elevation and incidence angle. Both are relatively easy to acquire from regional or national geoportals and GIS software, and hence the model can be directly applied to other locations. Accordingly, at each point of time, the probability of snow melt within a particular patch is assumed to be governed by just three factors: elevation ($E$) (a partial proxy for temperature), sun incidence angle ($I$), and the remaining snow coverage in neighbouring patches ($N$). Temperature and sun (largely, solar radiation) have been considered as drivers of snowmelt in a range of models (Zhou et al. 2021), while a dependency on the state of neighbouring cells is a fundamental feature of *CA* models (Ghosh et al. 2017); as such, our model forms a mixed cellular automaton (Pardo-Igúzquiza et al. 2017).

The model is calibrated against snow coverage masks estimated from Sentinel-2 satellite images. The employment of this relatively recent remote sensing product, already successfully used for creating high-resolution operational snow cover maps (Gascoin et al. 2019), limits some of the problems highlighted in a recent study that investigated the use of the *MODIS* product for snow detection (Bouamri et al. 2021).

Despite its relative simplicity, the model is capable of yielding an impressive fit against satellite data. A reasonable fit can even be obtained within a "bare-bones" framework that uses just $E$ and $N$, without considering $I$. A somewhat similar finding has been obtained by Saydi et al. (2019) when comparing the performance of a *Snowmelt Runoff Model* (*SRM*) that incorporates solar radiation with those based on a temperature-index, for the Urumqi River basin in the Xinjiang Uyghur Autonomous Region of China. Explicit consideration of solar radiation was found not to significantly improve model performance, since it is effectively a temperature-dependent energy source. However, we remark that when all three dependencies are included (i.e., also including the incidence angle), particularly within the extended *IEN*-model formulation, our model was capable of capturing additional subtle features of *SCA* changes. Our analysis reveals that $I$ plays

an important role during early stages of the process suggesting it provides the identification of regions that receive sufficient solar energy to trigger snowmelt. Inevitably any extensions carry a computational cost: stepping up from the basic to the extended model involves an almost doubling of the dimension of the parameter space, so the searching of suitable parameter sets becomes more challenging. Nevertheless, the extended model was still found to offer benefit in terms of improved fit to data, even for approximately equivalent computer resources (the same number of sample points). This suggests that further explorations would benefit from adoption of the extended model framework.

Of course, $E$, $I$ and $N$ constitute only a fraction of the factors that are likely to play a role in the snowmelt process. Many others (e.g. blown snow, frozen ground, rain-on-snow etc.) can be conceived, but at present the majority of models do not include such processes and thereby allow investigation into whether they will improve the accuracy of snowmelt simulations (Zhou et al. 2021). Indeed, in the context of the present site (expanded on further below), a number of discrepancies arise between the fitted model and the snow cover masks which could be attributed to missing key ingredients; in particular, we note that the catchment test site used in the present study is exposed to extreme winds, potentially accumulating snow or covering/uncovering particular patches.

Extending the model to include all potential factors that influence snowmelt – e.g. snow depth/density/structure – would, however, generate a complex model, with a high dimensional parameter space. In light of this, the *simplicity behind complexity* (Salcido 2011) feature of *CA* models allows a significant degree of complexity to be condensed into a single nondescript term, the neighbourhood. The assumption that melting in a neighbouring patch increases melting likelihood can be partly attributed to processes of surface albedo feedback and local heat transfer: surface albedo feedback drives warming at high elevations, with proximity to less reflective (and hence more energy absorbing) surfaces, such as grass, accelerating local snowmelt (Hernández-Henríquez et al. 2015, Ingram et al. 1989). Indeed, best-fitting parameter sets under the various models consistently require non-negligible weighting for the strength of neighbourhood influence, suggesting that this mechanism is a necessary component for a good-fitting model. Neighbourhood influence introduces nonlocality into the model, at a spatial scale linked to the spatial scale of patches. Here the patch dimensions are those of the employed snow cover masks ($\sim 14 \times 14\,\mathrm{m}^2$) and the neighbourhood constitutes just the four nearest neighbours (a von Neumann neighbourhood). An important future investigation, therefore, would be to explore neighbourhoods of different dimensions and observe how the weighting of neighbourhood dependence varies with the spatial scale of patches, e.g. through fitting against lower or higher resolution satellite data. In this regard, various studies (despite their different aims) have shown that such considerations can impact on the output of *CA* (e.g., Pan et al. 2010, Moreno et al. 2009, Chen and Mynett 2003). This in turn would provide further insight into the feasibility of using CAs to describe *SCA* changes across distinct spatial scales and locations: from the complex and fine scale catchment area considered here to the much larger areas explored in previous models (e.g. Pardo-Igúzquiza et al. 2017), or lower elevation sites, areas with smoother and more gradual slopes, distinct aspect etc.

Regarding the inputs, while elevation is a naturally fixed variable, the reduction of incidence angle to a constant-in-time function simplifies reality, where the position of the sun changes across the course of the day and year. Our streamlining process has involved setting incidence angle via a midday position at the initial stage in the snow-melt season; it would be possible, of course, to extend to a time-dependent incidence angle, although this would inevitably demand greater preprocessing of data. Encompassing time-variable inputs will expand the range of model application and, in particular, allow climatological variability to be included. For example, through extending to include temperature and precipitation variation, the model could be used to examine the sensitivity of snowmelt under a range of climate-change induced scenarios (Pardo-Igúzquiza et al. 2017,Collados-Lara et al. 2021), contributing towards *SDG13*.

Arriving at this stage will require further optimisation, and in particular a fitting of the model to describe how snow coverage fraction evolves over time. The present study has downplayed the temporal component, concentrating on the spatial characteristics of snow melt. Taking this further step would demand re-evaluation of certain model assumptions, in particular those placed on parameter $\rho$. $\rho$ can be viewed as an independent (i.e. independent of elevation *etc*) rate controlling parameter, where lower $\rho$ generates (on average) faster snowmelt at a particular site. We have treated $\rho$ as constant across the course of a simulation, but the hidden assumption here is that, for a patch surrounded by snow, the likelihood of snow melt when there is 10% coverage across the catchment will be the same as that when there is 90% coverage. This, of course, fails to acknowledge that a 10% SCA stage corresponds to much later in the summer, by which time mean air temperatures have considerably risen and snowmelt will be occurring at a greatly accelerated rate. This could be incorporated through extending $\rho$ to be a function of time, marking progression into warmer months.

The phenomenological nature of the model precludes direct estimation of parameters from experiments. This is somewhat a weakness of *CA* (and similar frameworks), in that the defining parameters do not straightforwardly link to a measurable quantity. An advantage, however, lies in that we subsequently assess the model according to its ability to fit data when parameters are randomly selected from a broad region of parameter space. The subsequent analysis showed that numerous parameter combinations yield a similar degree of fit (see Section D), suggesting that the model is not sensitive to a specific parameter combination, rather it is the relative weight of the various influencing factors that are of importance.

## 5. Conclusions

We have calibrated a *CA* model against estimated snow cover for the "Dora del Nivolet" catchment in the Gran Paradiso National Park, North Italy. The fitted model shows an impressive fit against data, recapitulating both general (for example, spatially extended melt tracts that form in the lower valley and extend upwards over time) and subtle (for example, localised melt and stripes on sun-facing slopes) features of the snowmelt process. However, some notable discrepancies remain between the *SCA* predicted in best-fitting simulations, and that deduced from satellite data. Notably, these discrepancies may be used to highlight some potential missing factors within the model, which we expand on below.

- The first (and probably the most prominent) model/data disparity lies in that the model predicts much faster snowmelt around the south-east corner of the catchment. From the perspective of the model, this is natural: the region has (relatively) low elevation, reasonable exposition to sun and lies adjacent to the region of initial snow melt. From the model assumptions, therefore, there is nothing to lead to delayed snowmelt for this region. Located at the upper end of the central valley through which the Dora del Nivolet runs, it is possible that prevailing winds act to channel precipitation and/or accumulate snow, leading to greater depth/density of snow. Further, mountain lakes here may generate local microclimates hard to be captured by the model.

- A second discrepancy lies in characterising the snowmelt across the more gently sloping terrain that leads up towards the south and west ridge boundaries of the catchment. Snow melt in this region appears to be highly intricate, with satellite data revealing a complex pattern of "fingering" as melt extends into the higher ground. While our model partially captures this fingering, it does not replicate the late stage "curving" of remaining snow stripes. Here, our model may be somewhat limited by its resolution and neighborhood configuration: each patch covers approximately $200\,\mathrm{m}^2$, elevation and incidence angle averaged across this area and the influence of just the four nearest neighbours is considered. It is possible, therefore, that more subtle variation in the nearby terrain may be at play.

- Overall,the present study downplays the temporal component, concentrating on the spatial characteristics of snowmelt. Therefore, it is to be expected that certain discrepancies will arise due to neglecting the temporal climatological variability across the study catchment.
- Finally, another possible source of discrepancy could be through the simple "binary" assumption, i.e. that patches are either snow or bare ground. Providing each patch with a continuous variable, e.g. representing the mass of snow covering a particular patch, would take the model in the direction of predicting how the spatial distribution of meltwater changes over spring and summer. Therefore, a further extension of the model would be to move beyond the current assumption of binary state patches.

Regardless of these caveats, we believe that the approach outlined in this paper provides a promising starting point for understanding the drivers of snow cover dynamics at a fine spatial scale, within complex topographical environments.

**Acknowledgements** This work was supported by the PRIN MIUR 2017SLJABC_005 WATZON Project. We warmly thank the support of the Valsavarenche Municipality and the Gran Paradiso National Park, in particular Bruno Bassano, Piero Chabod and Ramona Viterbi. We acknowledge "MIUR-Dipartimento di Eccellenza" funding to the Dipartimento Interateneo di Scienze, Progetto e Politiche del Territorio (DIST).

**Data sharing** MATLAB code and the necessary input data is available at the following site: `https://github.com/kjpainter/SnowMeltNivolet`

## References

Aalstad, K., Westermann, S., Bertino, L., 2020. Evaluating satellite retrieved fractional snow-covered area at a high-Arctic site using terrestrial photography. Remote Sensing of Environment 239, 111618.

Abudu, S., ping Sheng, Z., liang Cui, C., Saydi, M., Sabzi, H.Z., King, J.P., 2016. Integration of aspect and slope in snowmelt runoff modeling in a mountain watershed. Water Science and Engineering 9, 265–273.

Armstrong, R.L., Brun, E., 2008. Snow and Climate: Physical Processes, Surface Energy Exchange and Modeling.

Barry, R., Prévost, M., Stein, J., Plamondon, A.P., 1990. Application of a snow cover energy and mass balance model in a balsam fir forest. Water Resources Research 26.

Blöschl, G., Bierkens, M.F., Chambel, A., Cudennec, C., Destouni, G., Fiori, A., Kirchner, J.W., McDonnell, J.J., Savenije, H.H., Sivapalan, M., et al., 2019. Twenty-three unsolved problems in hydrology (UPH)–a community perspective. Hydrological Sciences Journal 64, 1141–1158.

Bouamri, H., Kinnard, C., Boudhar, A., Gascoin, S., Hanich, L., Chehbouni, A., 2021. MODIS does not capture the spatial heterogeneity of snow cover induced by solar radiation. Frontiers in Earth Science 9.

Butt, M.J., Bilal, M., 2011. Application of snowmelt runoff model for water resource management. Hydrological Processes 25, 3735–3747.

Chen, Q., Mynett, A.E., 2003. Effects of cell size and configuration in cellular automata based prey–predator modelling. Simulation Modelling Practice and Theory 11, 609–625.

Cochand, M., Christe, P., Ornstein, P., Hunkeler, D., 2019. Groundwater storage in high alpine catchments and its contribution to streamflow. Water Resources Research 55, 2613–2630.

Collados-Lara, A.J., Pardo-Igúzquiza, E., Pulido-Velazquez, D., 2021. Assessing the impact of climate change – and its uncertainty – on snow cover areas by using cellular automata models and stochastic weather generators. Science of The Total Environment 788, 147776.

D'Ambrosio, D., Di Gregorio, S., Gabriele, S., Gaudio, R., 2001. A cellular automata model for soil erosion by water. Physics and Chemistry of the Earth, Part B: Hydrology, Oceans and Atmosphere 26, 33–39.

Dedieu, J.P., Carlson, B.Z., Bigot, S., Sirguey, P., Vionnet, V., Choler, P., 2016. On the importance of high-resolution time series of optical imagery for quantifying the effects of snow cover duration on alpine plant habitat. Remote Sensing 8, 481.

DeWalle, D.R., Rango, A., 2008. Principles of Snow Hydrology. Cambridge University Press. doi:10.1017/CBO9780511535673.

Di Marco, N., Righetti, M., Avesani, D., Zaramella, M., Notarnicola, C., Borga, M., 2020. Comparison of modis and model-derived snow-covered areas: Impact of land use and solar illumination conditions. Geosciences 10, 134.

Dietz, A.J., Kuenzer, C., Gessner, U., Dech, S., 2012. Remote sensing of snow – a review of available methods. International Journal of Remote Sensing 33, 4094–4134.

Ditthakit, P., Pinthong, S., Salaeh, N., Binnui, F., Khwanchum, L., Kuriqi, A., Khedher, K.M., Pham, Q.B., 2021. Performance Evaluation of a Two-Parameters Monthly Rainfall-Runoff Model in the Southern Basin of Thailand. Water 13.

Dozier, J., 1989. Spectral signature of alpine snow cover from the landsat thematic mapper. Remote Sensing of Environment 28, 9–22.

Faye, C., 2022. Comparative Analysis of Meteorological Drought based on the SPI and SPEI Indices. HighTech and Innovation Journal 3, 15–27. Number: 0.

Gascoin, S., Barrou Dumont, Z., Deschamps-Berger, C., Marti, F., Salgues, G., López-Moreno, J.I., Revuelto, J., Michon, T., Schattan, P., Hagolle, O., 2020. Estimating fractional snow cover in open terrain from sentinel-2 using the normalized difference snow index. Remote Sensing 12, 2904.

Gascoin, S., Grizonnet, M., Bouchet, M., Salgues, G., Hagolle, O., 2019. Theia Snow collection: high-resolution operational snow cover maps from Sentinel-2 and Landsat-8 data. Earth System Science Data 11, 493–514.

Ghosh, P., Mukhopadhyay, A., Chanda, A., Mondal, P., Akhand, A., Mukherjee, S., Nayak, S., Ghosh, S., Mitra, D., Ghosh, T., et al., 2017. Application of cellular automata and markov-chain model in geospatial environmental modeling – A review. Remote Sensing Applications: Society and Environment 5, 64–77.

Gisolo, D., Previati, M., Bevilacqua, I., Canone, D., Boetti, M., Dematteis, N., Balocco, J., Ferrari, S., Gentile, A., N'sassila, M., Heery, B., Vereecken, H., Ferraris, S., 2022. A calibration free radiation driven model for estimating actual evapotranspiration of mountain grasslands (CLIME-MG). Journal of Hydrology 610, 127948.

Hall, D.K., Riggs, G.A., Salomonson, V.V., 1995. Development of methods for mapping global snow cover using moderate resolution imaging spectroradiometer data. Remote sensing of Environment 54, 127–140.

Härer, S., Bernhardt, M., Siebers, M., Schulz, K., 2018. On the need for a time- and location-dependent estimation of the NDSI threshold value for reducing existing uncertainties in snow cover maps at different scales. The Cryosphere 12, 1629–1642.

Hernández-Henríquez, M.A., Déry, S.J., Derksen, C., 2015. Polar amplification and elevation-dependence in trends of Northern Hemisphere snow cover extent, 1971–2014. Environmental Research Letters 10, 044010.

Hofmeister, F., Arias-Rodriguez, L.F., Premier, V., Marin, C., Notarnicola, C., Disse, M., Chiogna, G., 2022. Intercomparison of Sentinel-2 and modelled snow cover maps in a high-elevation Alpine catchment. Journal of Hydrology X 15, 100123.

Ingram, W.J., Wilson, C.A., Mitchell, J.F.B., 1989. Modeling climate change: An assessment of sea ice and surface albedo feedbacks. Journal of Geophysical Research: Atmospheres 94.

Javadinejad, S., Dara, R., Jafary, F., 2020. Climate Change Scenarios and Effects on Snow-Melt Runoff. Civil Engineering Journal 6, 1715–1725. Number: 9.

Jenicek, M., Ledvinka, O., 2020. Importance of snowmelt contribution to seasonal runoff and summer low flows in Czechia. Hydrology and Earth System Sciences 24, 3475–3491.

Karafyllidis, I., Thanailakis, A., 1997. A model for predicting forest fire spreading using cellular automata. Ecological Modelling 99, 87–97.

Kumar, R., Manzoor, S., Vishwakarma, D.K., Al-Ansari, N., Kushwaha, N.L., Elbeltagi, A., Sushanth, K., Prasad, V., Kuriqi, A., 2022. Assessment of Climate Change Impact on Snowmelt Runoff in Himalayan Region. Sustainability 14, 1150.

Kundzewicz, Z.W., 2008. Climate change impacts on the hydrological cycle. Ecohydrology & Hydrobiology 8, 195–203.

Largeron, C., Dumont, M., Morin, S., Boone, A., Lafaysse, M., Metref, S., Cosme, E., Jonas, T., Winstral, A., Margulis, S.A., 2020. Toward snow cover estimation in mountainous areas using modern data assimilation methods: A review. Frontiers in Earth Science 8.

Leavesley, 1989. Problems of snowmelt runoff modelling for a variety of physiographic and climatic conditions. Hydrological Sciences Journal 34, 617–634.

Leguizamón, S., 2005. Simulation of snow-cover dynamics using the cellular automata approach. Proc. of the 8th Int. Symposium on High Mountain Remote Sensing Cartography .

Liang, T.G., Huang, X.D., Wu, C.X., Liu, X.Y., Li, W.L., Guo, Z.G., Ren, J.Z., 2008. An application of MODIS data to snow cover monitoring in a pastoral area: A case study in Northern Xinjiang, China. Remote Sensing of Environment 112.

Ma, Y.P., Sudakov, I., Strong, C., Golden, K.M., 2019. Ising model for melt ponds on arctic sea ice. New Journal of Physics 21, 063029.

Masson, T., Dumont, M., Mura, M.D., Sirguey, P., Gascoin, S., Dedieu, J.P., Chanussot, J., 2018. An assessment of existing methodologies to retrieve snow cover fraction from modis data. Remote Sensing 10, 619.

McKay, M.D., Beckman, R.J., Conover, W.J., 1979. A comparison of three methods for selecting values of input variables in the analysis of output from a computer code. Technometrics 42, 55–61.

Mohammadi, B., Safari, M.J.S., Vazifehkhah, S., 2022. IHACRES, GR4J and MISD-based multi conceptual-machine learning approach for rainfall-runoff modeling. Scientific Reports 12, 12096.

Moreno, N., Wang, F., Marceau, D.J., 2009. Implementation of a dynamic neighborhood in a land-use vector-based cellular automata model. Computers, Environment and Urban Systems 33, 44–54.

Pan, Y., Roth, A., Yu, Z., Doluschitz, R., 2010. The impact of variation in scale on the behavior of a cellular automata used for land use change modeling. Computers, Environment and Urban Systems 34, 400–408. doi:10.1016/j.compenvurbsys.2010.03.003.

Pardo-Igúzquiza, E., Collados-Lara, A.J., Pulido-Velazquez, D., 2017. Estimation of the spatiotemporal dynamics of snow covered area by using cellular automata models. Journal of Hydrology 550, 230–238.

Planchon, O., Darboux, F., 2002. A fast, simple and versatile algorithm to fill the depressions of digital elevation models. CATENA 46, 159–176.

Richter, R., Schläpfer, D., 2011. Atmospheric/topographic correction for satellite imagery: Atcor-2/3 userguide .

Salcido, A., 2011. Cellular Automata: Simplicity Behind Complexity.

Salomonson, V.V., Appel, I., 2004. Estimating fractional snow cover from modis using the normalized difference snow index. Remote Sensing of Environment 89, 351–360.

Salzano, R., Lanconelli, C., Esposito, G., Giusto, M., Montagnoli, M., Salvatori, R., 2021. On the Seasonality of the Snow Optical Behaviour at Ny Ålesund (Svalbard Islands, Norway). Geosciences 11, 112.

Saydi, M., Ding, J.l., Sagan, V., Qin, Y., 2019. Snowmelt modeling using two melt-rate models in the Urumqi River watershed, Xinjiang Uyghur Autonomous Region, China. Journal of Mountain Science 16, 2271–2284.

Singh, A.K., Kumar, P., Ali, R., Al-Ansari, N., Vishwakarma, D.K., Kushwaha, K.S., Panda, K.C., Sagar, A., Mirzania, E., Elbeltagi, A., Kuriqi, A., Heddam, S., 2022. An Integrated Statistical-Machine Learning Approach for Runoff Prediction. Sustainability 14, 8209.

Tarboton, D.G., Bras, R.L., Rodriguez-Iturbe, I., 1991. On the extraction of channel networks from digital elevation data. Hydrological Processes 5, 81–100.

Thackeray, C.W., Fletcher, C.G., 2016. Snow albedo feedback: Current knowledge, importance, outstanding issues and future directions. Progress in Physical Geography: Earth and Environment 40, 392–408.

Vikhamar, D., Solberg, R., 2003. Snow-cover mapping in forests by constrained linear spectral unmixing of modis data. Remote Sensing of Environment 88, 309–323.

Xiao, M., 2021. A warning of earlier snowmelt. Nature Climate Change 11.

Yin, D., Cao, X., Chen, X., Shao, Y., Chen, J., 2013. Comparison of automatic thresholding methods for snow-cover mapping using Landsat TM imagery. International Journal of Remote Sensing 34, 6529–6538.

Zhou, G., Cui, M., Wan, J., Zhang, S., 2021. A review on snowmelt models: Progress and prospect. Sustainability 13.

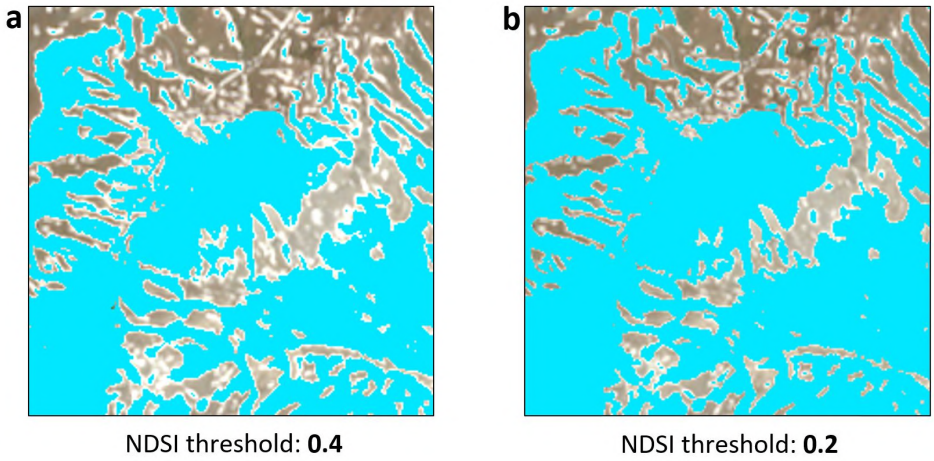


Figure 8: **a** Snow pixels classification using a NDSI threshold of 0.4 over a sample area within the Dora del Nivolet catchment. Snow cover is represented in bright vivid blue. White pixels that protrude from the snow cover mask indicate real snowy areas, thus suggesting an underestimated snow cover area. **b** Snow pixels classification using a NDSI threshold of 0.2 over a sample area within the Dora del Nivolet catchment. A larger amount of real snowy areas are thereby included in the snow cover mask.

# Appendices

### A. Calibration of the NDSI threshould

In Fig. 8 we illustrate the improved estimation of snow cover area following the manual calibration of the NDSI threshold.

### B. Tables for symbols and model inputs

In Table 2 we provide a list of symbols/acronyms used during the text. In Table 3 we provide a list of variables, inputs and parameters for the *CA* model formulated in Section 2.2.

### C. Simulation algorithm

The simulation code is implemented in MATLAB. Essentially, in each time step: (i) remaining snow-covered patches are located and randomly ordered into a sequence ($\mathcal{S}$); (ii) for the first patch in the sequence, its melt probability is calculated according to Equation (1) and a uniform random number between 0 and 1 is generated to determine whether melting occurs; (iii) we proceed through the sequence until all elements in $\mathcal{S}$ have been tested; (iv) time is updated time and we return to (i). Code is available at GitHub and a pseudo-algorithm is provided below. We note that while parameter ranges were chosen such that simulations would generally be computable within a reasonable timeframe, certain combinations may push the model into a regime requiring exorbitant c.p.u. time (via minuscule probability of snowmelt in certain regions). The maximum number of total time steps for a particular simulation was therefore capped (here, at $10^5$) to prevent simulation jams of this nature and parameter set combinations falling foul are excluded.

### D. Error analysis of the IEN-model and default $\lambda$

We briefly summarise the analysis following the randomised search of parameter space, focusing on the basic IEN-model. As described in methods, for each sample parameter set the model is simulated 5 times and errors are computed according to Eq. (5) under varying $\lambda$ and using

| | |
|---|---|
| ***AC*** | *Atmospheric Correction* |
| ***CA*** | *Cellular Automata* |
| ***DEM*** | *Digital Elevation Model* |
| ***DOY*** | *Day Of Year* |
| ***DTM*** | *Digital Terrain Model* |
| ***E*** | *(patch) Elevation* |
| $f_{SCA}$ | *fractional Snow Cover Area* |
| ***ESA*** | *European Space Agency* |
| ***I*** | *(patch) sun Incidence angle* |
| ***L1C*** | *Level-1C Sentinel-2 product* |
| ***L2A*** | *Level-2A Sentinel-2 product* |
| ***N*** | *(patch) proportion of Nearby snow coverage* |
| ***NDSI*** | *Normalised Difference Snow Index* |
| ***POI*** | *Period of Interest* |
| ***RCP*** | *Representative Concentration Pathways* |
| ***SCA*** | *Snow-Covered Area* |
| ***SDG*** | *Sustainable Development Goals* |

Table 2: Acronyms and symbols used in the text.

| Notation | Range/value | Interpretation |
|---|---|---|
| $a(x)$ | $[0, 1]$ | incidence angle (rescaled) of patch centred at $x$ |
| $e(x)$ | $[0, 1]$ | elevation (rescaled) of patch centred at $x$ |
| $b(x, t)$ | $[0, 1]$ | proportion of nearby snow coverage of patch centred at $x$ at time $t$ |
| $S(x, t)$ | $\{0, 1\}$ | state of patch (0 = grass, 1 = snow) centred at $x$ at time $t$ |
| $\rho$ | $[2, 10]$ | independent snow melt likelihood |
| $\alpha$ | $[0, 9]$ | weighting for impact of incidence angle |
| $\beta$ | $[0, 9]$ | weighting for impact of elevation |
| $\gamma$ | $[0, 9]$ | weighting for impact of nearby snow coverage |
| $p$ | $[0, 3]$ | nonlinearity parameter for incidence angle |
| $q$ | $[0, 3]$ | nonlinearity parameter for elevation |
| $r$ | $[0, 3]$ | nonlinearity parameter for nearby snow coverage |
| $\Delta x$ | $\sim 14$ (metres) | patch dimensions |
| $\Delta t$ | 1 (unitless) | time step |

Table 3: List of inputs, variables, functions and parameters for the *CA* model.

**Algorithm 1** Pseudo algorithm for model implementation

```
t=0
while (continue until stopping condition satisfied) do
    find the set of snow-covered patches
    randomly order this set into a sequence 𝒮
    for i=1..size(S) do
        select patch x_i
        calculate P(x_i)
        If X < P(x_i), s(x_i) = 0 (X a uniform random number between 0 and 1)
    end for
    t = t + Δt
end while
```

the full set of snow masks in the calibration, i.e. Eq. (6). Fig. 9 charts statistics of this analysis, where from top to bottom row we vary $\lambda$ from 1 (only coincidence-based error) to 0 (only interface-based error). The left panels in Fig. 9 chart errors (means $\pm$ standard deviation). Notably, we observe small standard deviations, indicating low variation about the mean error for each simulation at a specific parameter set and suggesting 5 simulations for each parameter set is sufficient to obtain a reasonable error estimate. Restricting to the mean errors computed across the top 1% of parameter sets generates good fitting parameter sets with mean errors lying within a few percent of each other.

To determine a suitable default value for $\lambda$ we (i) explore the values of the weighting parameters across the top 1% parameter sets at each $\lambda$, and (ii) examine representative simulation output from top performing sets at each $\lambda$. The weighting parameters for the top 1% sets are shown in the right hand panels of Fig. 9. Notably, we observe broadly consistent results for $\lambda$ between 0.5 and 1, indicating a commonality between the parameter sets contributing to the top 1% sets. For lower $\lambda$, however, significantly different weighting parameters are observed, along with more variance. This is substantiated when examining representative simulation output for top performing sets, where Fig. 10 shows the simulation output at 59.1% snow coverage, for the top 5 ranked parameter sets under each $\lambda$. Subtle distinctions aside, simulations in the top 3 rows are highly consistent and provide a reasonable match against the snow coverage estimated from satellite images at an equivalent stage. Low $\lambda$, however, generate less consistent results, with some highly ranked parameter sets producing debatable match against the data (e.g. see bottom left panel). Accordingly, we use a value of $\lambda = 0.75$ that generates both good calibration against the experimental data set and provides reasonably consistency across simulations with varying parameters.

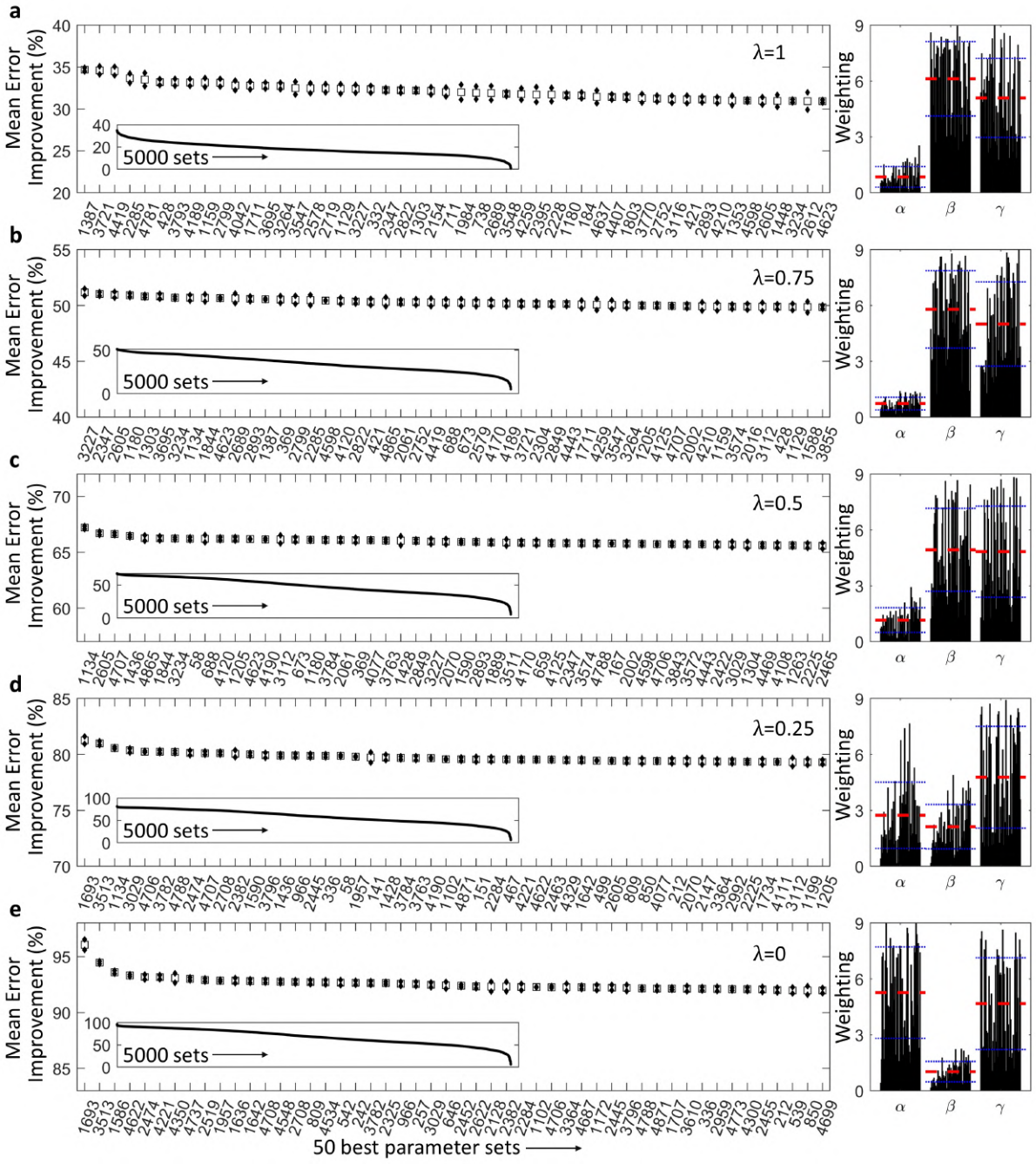


Figure 9: Error analysis for 5000 randomly sampled parameter sets for the basic IEN-model, calibrated against satellite data according to Eq. (5) with Eq. (6) and **a** $\lambda = 1$, **b** $\lambda = 0.75$, **c** $\lambda = 0.5$, **d** $\lambda = 0.25$, **e** $\lambda = 0$. (Left column, main axis) Mean error $\pm$ standard deviation for the top 50 fitting parameter sets, reported as the error improvement over the null model; (Left column, inset axis) Mean error for the full 5000 sets. (Right column) Weighting parameters $(\alpha, \beta, \gamma)$ for the top 50 parameter sets, along with their mean values (red dashed) $\pm$ standard deviations (blue dotted).

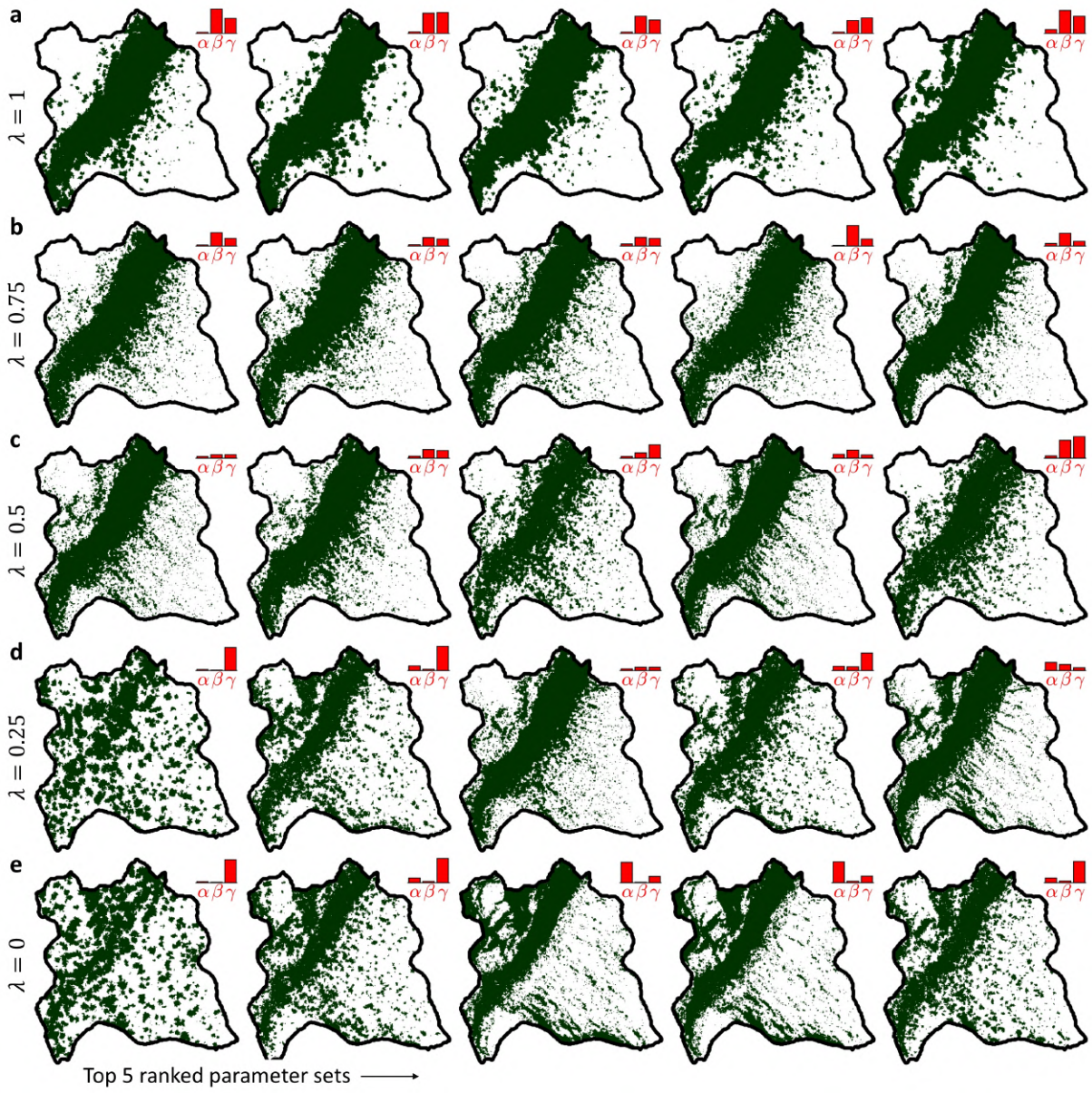


Figure 10: Representative simulation output for the 5 best parameter sets, selected following the error analysis reported in Fig. 9, with the ranking according to Eq. (5) for **a** $\lambda = 1$, **b** $\lambda = 0.75$, **c** $\lambda = 0.5$, **d** $\lambda = 0.25$, **e** $\lambda = 0$. Output shown at the 59.1% snow coverage stage, with the weighting parameters for each simulation indicated by the bar chart at the top right.

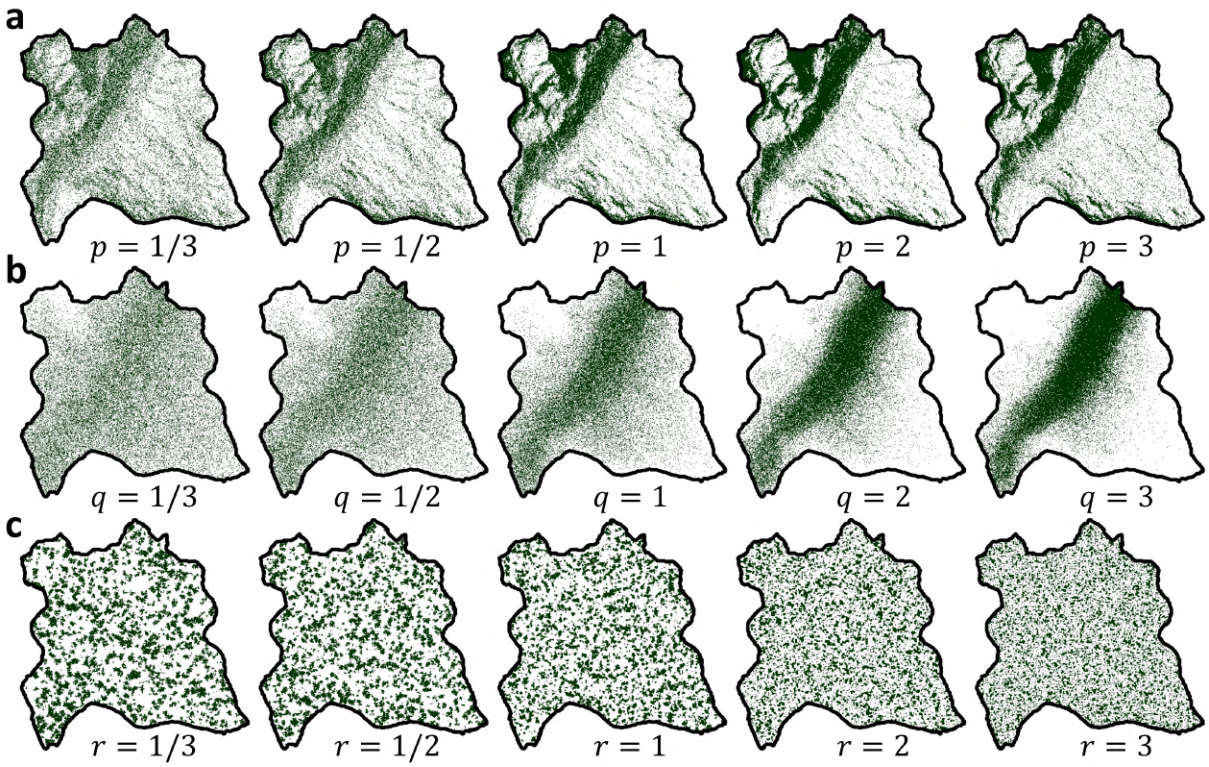


Figure 11: Representative simulations showing the greater subtlety generated through the extended model formulation, i.e. Eq. (2) with varying $(p, q, r)$. **a** As $p$ is varied, we see either dispersion or concentration of the spatial heterogeneity stemming from variable incidence angle (other parameters $\alpha = 5$, $\beta = \gamma = q = r = 0$, $\rho = 20/3$). **b** As $q$ is varied, we see either dispersion or concentration of the spatial heterogeneity stemming from variable elevation (other parameters $\beta = 5$, $\alpha = \gamma = p = r = 0$, $\rho = 20/3$). **c** As $r$ is varied, we see a variation in the characteristic spatial scale of melt patches due to neighborhood dependency (other parameters $\gamma = 5$, $\alpha = \beta = p = q = 0$, $\rho = 20/3$). Note that simulation output corresponds to the stage with 70.3% remaining snow coverage.